

Article

The Zircon U-Pb Age, Hf Isotopes, and Lithogeochemistry of Ore-Bearing Rocks from the Archean Hongtoushan Volcanogenic Massive Sulfide Deposit in the North China Craton: Implications for Tectonic Setting

Xinwei You ¹, Ende Wang ^{1,*}, Yekai Men ^{1,2}, Jianfei Fu ¹, Kun Song ³ and Sishun Ma ¹

¹ School of Resources and Civil Engineering, Northeastern University, Shenyang 110819, China; air910305@gmail.com (X.Y.); menyekai@163.com (Y.M.); fujianfei@mail.neu.edu.cn (J.F.); masishun@stumail.neu.edu.cn (S.M.)

² School of Resource & Materials, Northeastern University at Qinhuangdao, Qinhuangdao 066004, China

³ School of Earth and Space Sciences, Peking University, Beijing 100871, China; songkun1992@pku.edu.cn

* Correspondence: wnd@mail.neu.edu.cn

Abstract: Volcanogenic massive sulfide (VMS) deposits are globally significant sources of metals. The Hongtoushan VMS deposit is the only large Archean Cu-Zn VMS deposit in the North China Craton, carrying substantial economic value. Significant deformation and metamorphism have made the tectonic setting of the Hongtoushan VMS deposit the subject of extensive debate. This study investigates the petrogenesis and chronology of the ore-bearing host rocks from the Hongtoushan Cu-Zn VMS deposit in the North China Craton. By utilizing whole-rock geochemical analyses and zircon dating, this research sheds light on the origin and evolution of the ore-bearing rocks within the deposit. The whole-rock geochemical analysis data indicate that the Hongtoushan ore-bearing rock series is mainly composed of amphibole plagioclase gneiss (basalt protolith) and biotite plagioclase gneiss (andesite and rhyolite protolith), suggesting a complete volcanic cycle from basic to medium-acidic volcanic rocks. The amphibole plagioclase gneiss has slight LREE enrichment patterns with unremarkable depletions of Nb, Ta, and Ti and belongs to contaminated ocean plateau basalt (OPB) in terms of composition, which is generally interpreted as being generated from the mantle plume head. Meanwhile, the biotite plagioclase gneiss has relatively steep LREE enrichment distribution patterns with remarkable negative Ta, Nb, and Ti anomalies and a wide range of Zr/Y ratios, indicating their classification as FI- and FII-type felsic rocks; they were likely formed through the fractional crystallization of basic magma combined with crustal assimilation. When combined with the zircon dating results, the ore-bearing host rocks of the Hongtoushan VMS deposit were generated via a continuous magmatic evolution process. The zircon dating of the host rocks indicates a formation age of between 2609 and 2503 Ma, with metamorphic events between 2540 and 2466 Ma, which is consistent with the 2.5 Ga-related global mantle plume event. Further research shows that the ore-bearing host rocks are more likely to have been formed in a mantle plume-related stretching environment, possibly a margin rift.

Keywords: zircon U-Pb; VMS; mantle plume; subduction; geochemistry; North China Craton



Citation: You, X.; Wang, E.; Men, Y.; Fu, J.; Song, K.; Ma, S. The Zircon U-Pb Age, Hf Isotopes, and Lithogeochemistry of Ore-Bearing Rocks from the Archean Hongtoushan Volcanogenic Massive Sulfide Deposit in the North China Craton: Implications for Tectonic Setting. *Minerals* **2024**, *14*, 367. <https://doi.org/10.3390/min14040367>

Academic Editors: Wenlei Song, Xiaohua Deng, Zhanke Li and Alexey V. Ivanov

Received: 25 January 2024

Revised: 14 March 2024

Accepted: 24 March 2024

Published: 29 March 2024



Copyright: © 2024 by the authors. Licensee MDPI, Basel, Switzerland. This article is an open access article distributed under the terms and conditions of the Creative Commons Attribution (CC BY) license (<https://creativecommons.org/licenses/by/4.0/>).

1. Introduction

The Qingyuan granitic-greenstone belt (QGB) was the first identified Archean greenstone belt in China. Numerous Cu-Zn deposits of varying sizes have been discovered in the QGB, serving as significant sources of copper, zinc, and lead in China. As the largest volcanogenic massive sulfide (VMS) deposit in the QGB, the Hongtoushan VMS deposit has been exploited until now. The Hongtoushan Cu-Zn deposit has been the focus of much research due to its unique metallogenetic environment and model. Significant geological

and geochemical research has been conducted on the Hongtoushan VMS deposit since its discovery in 1957 [1,2], resulting in its classification as a VMS-type deposit and its designation as the “Hongtoushan type” by Chinese geologists [3].

The ancient Archean Hongtoushan VMS deposit has experienced significant deformation and metamorphism, leading to the development of ore bodies with intricate and complex geometries [4,5]. The tectonic setting of the Hongtoushan VMS deposit has been the subject of extensive debate. Previous scholars have proposed multiple hypotheses, which can be broadly categorized into two main schools of thought: the magmatic arc model and the mantle plume model. However, these two schools of thought are somewhat inconsistent with each other and have failed to explain certain factors based on field geological and geochemical data.

Supporters of the mantle plume model, such as Franklin et al. (2005) [6], argue that VMS mineralization universally requires a submarine heat source in an extensional tectonic setting, including oceanic environments or marine basins developed on rifted crusts. Zhai et al. (1985) [1] proposed that the supracrustal volcanic rocks (greenstone belt) erupted in a paleo-continental rift above a hotspot (mantle plume), whereas Wu et al. (2013) [7] suggested that the terrain was formed above a mantle plume based on lithological characteristics and anti-clockwise pressure–temperature paths involving a period of isobaric cooling. However, these theories face a compelling question in terms of explaining the magmatic arc characteristics of the host rocks in the Hongtoushan deposit. On the other hand, proponents of the magmatic arc model, such as Li et al. (2000) and Wan et al. (2005) [8,9], argue that the QGB evolved in a continental arc environment followed by arc collision. However, in the eastern North China Craton (NCC), Neoarchean magmatism extends over a width of more than 800 km [10], and the prominent structural feature is the dome-and-keel structure [11], which is inconsistent with subduction processes.

In order to shed light on the origin and tectonic setting of the Hongtoushan VMS deposit, this study investigates the petrogenesis and zircon chronology of the ore-bearing host rocks from the Hongtoushan Cu-Zn VMS deposit in the North China Craton, contributing to the understanding of the geological processes involved in the formation of Hongtoushan VMS deposits and tectonic evolution in the Archean period.

2. Local Geology

2.1. Regional Geology

The Hongtoushan Cu-Zn VMS deposit is situated within the Qingyuan granite-greenstone belt, which forms a part of the North China Craton (NCC) (Figure 1A). The NCC encompasses an Archean to Paleoproterozoic metamorphic basement overlayed by Mesoproterozoic to Cenozoic unmetamorphosed cover. The metamorphic basement rocks exhibit ages ranging from 3.8 to 3.2 Ga [9,12,13]. Neoarchean metamorphic rocks are predominantly composed of 2.6–2.5 Ga tonalite–trondhjemite–granodiorite (TTG) gneisses, ~2.5 Ga syntectonic granites and various supracrustal rocks that experienced greenschist to granulite facies in regional metamorphism and polyphase deformation around 2.5 Ga [14–16]. The NCC is divided into two major Archean to Paleoproterozoic blocks, the eastern and western blocks, separated by the Paleoproterozoic Trans-North China orogenic belt [17]. The Qingyuan greenstone belt is located at the northern margin of the eastern block and, together with large volumes of granitoid compositions, it is commonly known as the Qingyuan Group [9,18] (Figure 1B). The Qingyuan Group is divided into the Hunbei and Hunnan terranes by the Hunhe fault [19,20]. The greenstone in the Hunbei terrane comprises a sequence of gneiss and amphibolite that is further classified into the Shipengzi, Hongtoushan, and Nantianmen formations, which experienced amphibolite to granulite facies metamorphism between 2.9 and 2.8 Ga [1,19]. The VMS deposit is the predominant mineral resource in the Qingyuan greenstone belt, wherein the Hongtoushan VMS deposit stands out as the largest in the region. The size and location of Cu-Zn mineralization in the area are controlled by impermeable volcanic layers [21].

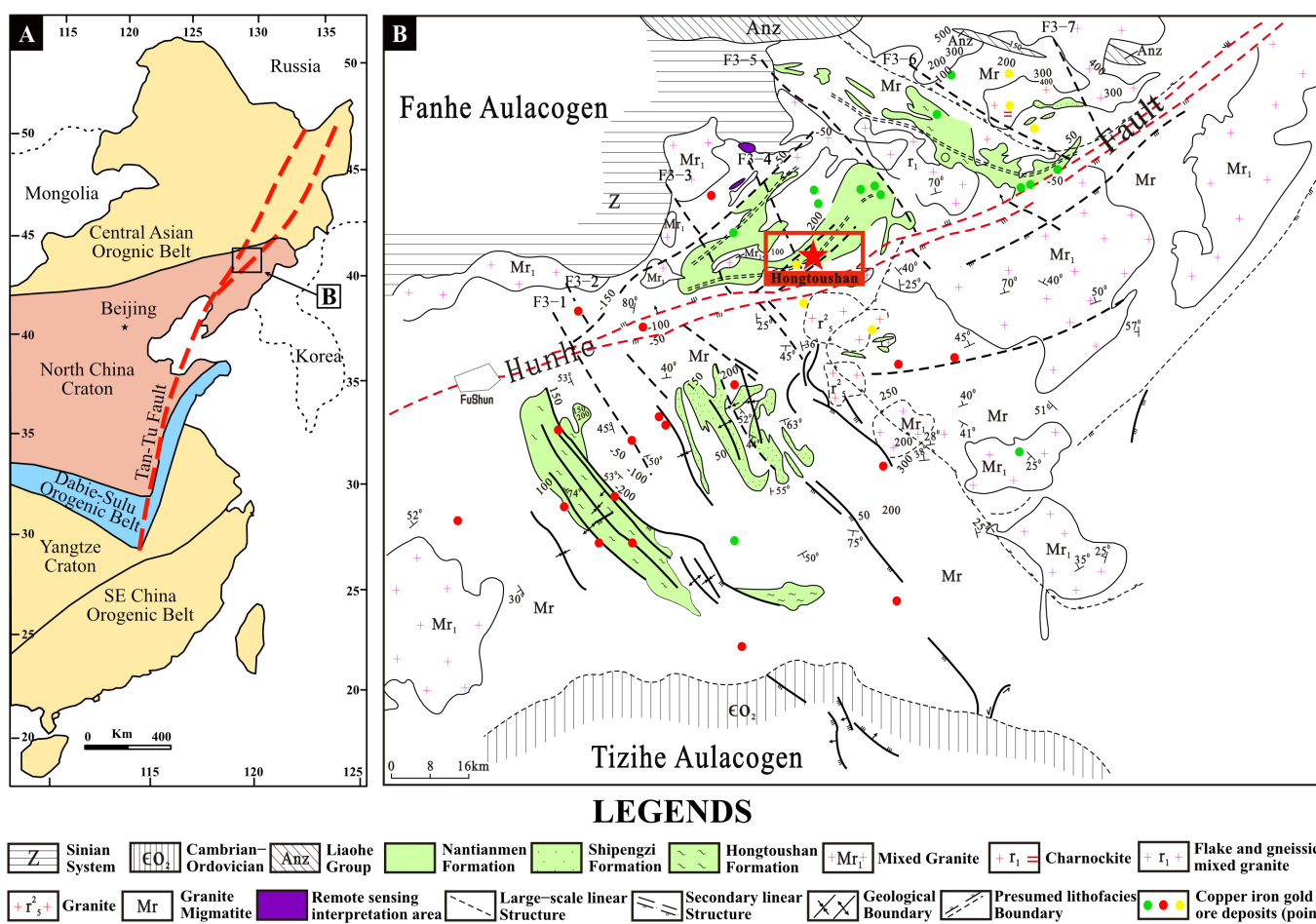


Figure 1. (A) The distribution of the basement in the North China Craton. (B) Regional geological map of the Qingyuan greenstone belt (after Fengjin Yu, (2005) [22]).

2.2. Ore Deposit Geology

The Hongtoushan VMS deposit is a significant Archean VMS Cu-Zn deposit located in the Hunbei district. Local residents began the surface mining of the deposit in the early 1930s, and large-scale underground operations started in the 1960s following systematic drilling. The deposit has a metal reserve of 0.5 Mt Cu at 1.5% to 1.8% Cu, 0.7 Mt Zn at 2.0% to 2.5% Zn, 20 t Au at 0.5 to 0.8 g/t Au, and 1000 t Ag at 20 to 60 g/t Ag, respectively [2]. Mining operations have reached a depth of 1337 m [23].

The primary ore deposits in the area are confined within the “rhythmic member” of the upper section of the Hongtoushan formation, which is mainly composed of biotite plagioclase gneiss and hornblende plagioclase gneiss and can be divided into seven layers. From top to bottom, these layers include (1) a 12 m-thick layer of biotite gneiss and quartz-feldspar gneiss with intercalations of plagioclase hornblende gneiss; (2) a 25 m-thick layer of garnet quartz plagioclase gneiss intercalated with granulite; (3) a 20 m-thick layer of plagioclase amphibole gneiss and biotite plagioclase gneiss intercalations; (4) a 20 m-thick layer of plagioclase hornblende gneiss intercalated with thin biotite plagioclase gneiss; (5) a 20 m-thick layer of biotite plagioclase gneiss with plagioclase hornblende gneiss; and (6) a 10 m-thick layer of plagioclase hornblende gneiss, biotite plagioclase gneiss, and interbedded plagioclase hornblende gneiss (Figure 2G). Petrological and geochemical investigations indicate that the protolith of meta-volcanic rocks in the Jinfengling and Hongtoushan formations is tholeiitic to calc-alkalic volcanic rocks [1,4].

The massive sulfide ores in the area are hosted by rocks that have undergone upper amphibolite facies metamorphism [24]. The surrounding rocks are mainly composed of amphibolite gneiss, sillimanite-biotite gneiss, and biotite plagioclase gneiss, and the pro-

toliths are believed to be continuously differentiated volcanic rocks varying in composition from basic to intermediate acid volcanic rocks [5] (Figure 2G).

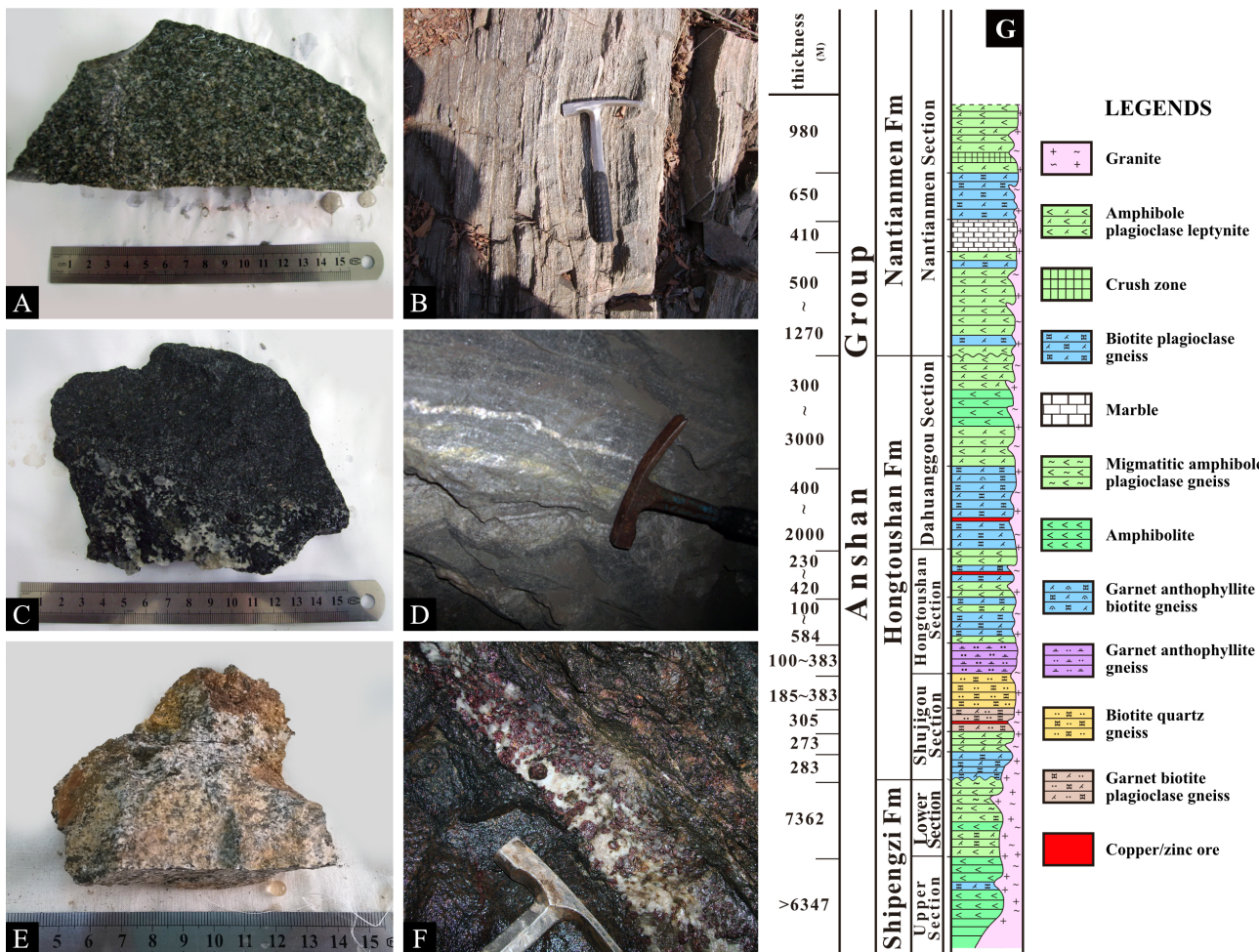


Figure 2. (A) Hornblende-plagioclase gneiss; (B) sillimanite biotite plagioclase gneiss; (C) biotite plagioclase gneiss; (D) biotite plagioclase gneiss in the field; (E) garnet anthophyllite gneiss; (F) re-crystallized garnet in garnet anthophyllite gneiss. (G) Stratigraphic column of Hongtoushan VMS deposit (after Fengjin Yu, (2005) [22]).

The Archean Qingyuan greenstone belt has undergone multiple episodes of deformation, metamorphism, intrusion by granites, and migmatization, resulting in the Hongtoushan VMS deposit having a highly intricate structure. Above a depth of ~467 m, the ore bodies display a Y-shaped structure, where the two branches extend towards the east. As they progress, these two branches combine and form a unified entity towards the west (Figure 3A,C). According to previous research results [22,23], three periods of tectonic deformation have been identified in the Hongtoushan VMS deposit. In the initial phase, the north-south tight fold was generated in response to the east-west extrusion force. Following this, the north-south extrusion force led to the formation of the east-west plunging vertical fold in the subsequent stage. Under tectonic compression, the original ore body migrated from the limbs towards the hinge zone, resulting in the thickening and upgrading of the ore body and the formation of the “ore pillar” (Figure 3B). Lastly, driven by east-west extrusion and north-south torsion, the third stage culminated in the development of the north-south open fold. Fold deformation transforms the occurring forms of the ore body and plays an ore-controlling and ore-hosting role in the transformation.

The deposit can be classified into two types of ores: massive and disseminated ore. The dominant ore minerals are pyrite, pyrrhotite, sphalerite, and chalcopyrite, with minor amounts of magnetite, galena, molybdenite, argentite, and electrum. The gangue min-

erals mainly consist of quartz, plagioclase, biotite, phlogopite, sericite, garnet, gahnite, sillimanite, and other minerals. The wall rock alteration is characterized by tremolitization, phlogopitization, sericitization, silicification, chloritization, and carbonation (Figure 4).

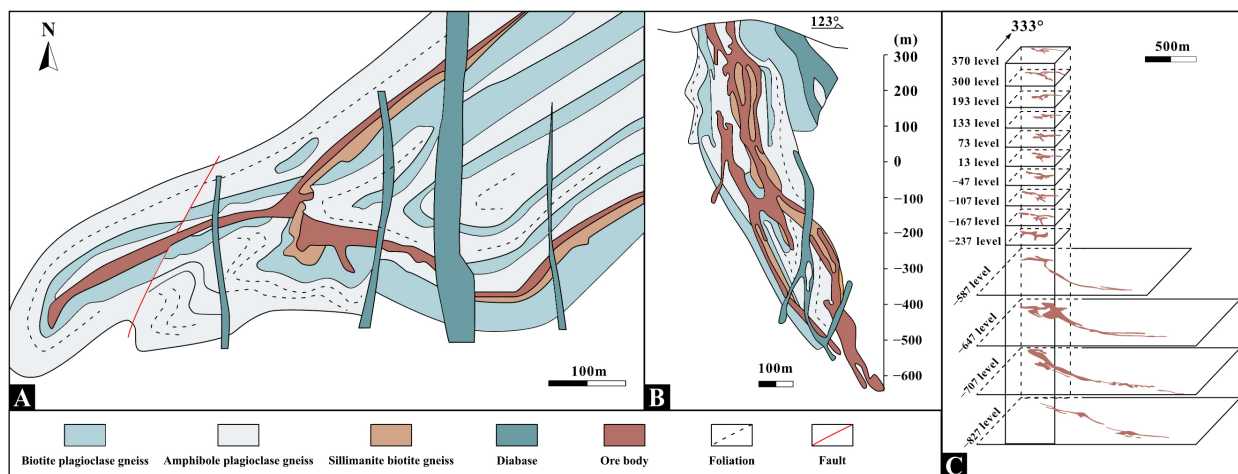


Figure 3. (A,B) Geological map and section map of No. 14 prospecting line in the Hongtoushan VMS deposit at the -167 m level (after Zhu, 2015 [25]). (C) Stereoscopic map of the ore body of the Hongtoushan VMS deposit (modified by Zhang, 2010 [5]).

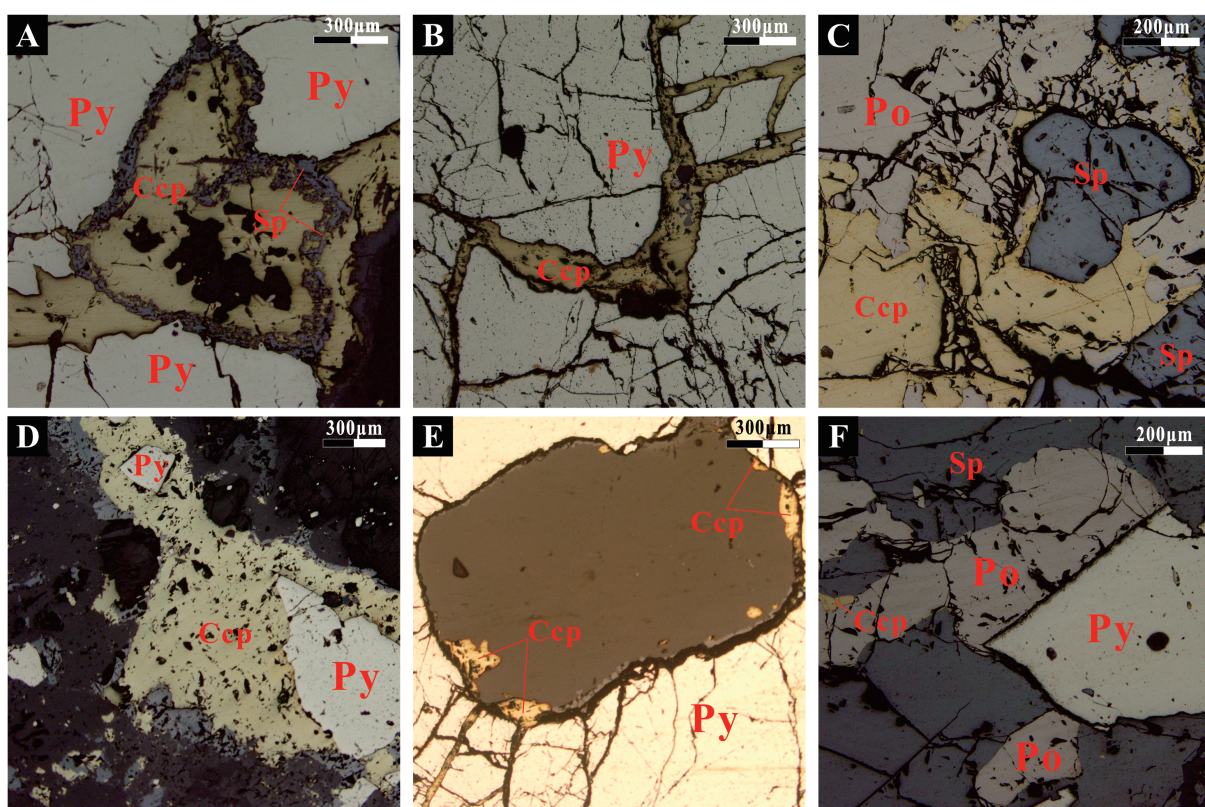


Figure 4. (A,B) Cataclastic texture: the cracks of pyrite filled by plastic chalcopyrite; (C) porphyritic texture of pyrite; (D) different species of pyrite: cubic and granular in chalcopyrite surrounded by sphalerite; (E) chalcopyrite and pyrrhotite fill the fractures between pyrite and quartz; (F) the coexistence of Pyrite, chalcopyrite, sphalerite and pyrrhotite.(abbreviations: Py = pyrite; Po = pyrrhotite; Ccp = chalcopyrite; Sp = sphalerite).

3. Samples and Analytical Methods

3.1. Sample Descriptions

The samples were collected from ore-bearing metamorphic rocks (the rhythmic member) (Figure 2A–F) and classified into two major categories according to mineral composition: amphibole plagioclase gneiss and biotite plagioclase gneiss. For these two groups of rocks, we proceeded to conduct a comprehensive suite of analyses. In total, 20 rock samples were selected for major and trace (rare earth) element analyses, while subsequent preliminary microscopic observations confirmed the presence of a sufficient number of zircon grains. Six rock samples (including three amphibole plagioclase gneiss and three biotite plagioclase gneiss samples) were finally chosen for zircon U-Pb dating and a Hf isotope analysis.

3.2. Analytical Methods

3.2.1. Whole-Rock Geochemistry Analysis

Whole-rock major and trace (rare earth) element analyses were performed at the Geoanalytical Center of Nuclear Industry in Beijing using X-ray fluorescence (XRF) spectrometry and inductively coupled plasma mass spectrometry (ICP-MS), respectively. The analytical uncertainties for major elements are 1%~3%, and this is based on the GB/T14506.28-2010 standard [26]. For trace element and rare earth element analyses, in accordance with the DZ/T0223-2001 standard [27], rock powders (50 mg) were dissolved using mixed acids (HF + HClO₄) in capped Savillex Teflon beakers at 120 °C for 6 days and were subsequently dried to wet salt and then re-dissolved in 0.5 mL HClO₄. The solutions were then evaporated to wet salt at 140 °C and re-dissolved in 1 mL HNO₃ and 3 mL water for 24 h at 120 °C. The solutions were diluted in 2% HNO₃ for analysis. The uncertainties based on the replicate analyses of internal standards are ±5% for REE and ±5%~10% for trace elements.

3.2.2. Zircon CL Images and U-Pb Dating

Zircon grains were isolated from whole-rock samples through a magnetic and heavy liquid separation technique at Beijing GeoAnalysis Co., Ltd., Beijing, China. These zircon grains were subsequently randomly embedded in epoxy mounts, and then the mounts were polished for sectioning. Detailed documentation of all zircon grains was carried out using transmitted and reflected light micrographs, along with cathodoluminescence (CL) images, to elucidate their internal structures. The CL images of the zircon grains were captured at Beijing GeoAnalysis Co., Ltd. by utilizing a JEOL IT-500 SEM equipped with a Delmic CL system.

Zircon U-Pb dating was performed using a Resolution SE-type 193 nm deep-ultraviolet laser ablation sampling system (Applied Spectra, Fremont, CA, USA) and an S155-type double-volume sample cell at Beijing GeoAnalysis Co., Ltd. A fixed 30 μm diameter laser beam was utilized with a laser pulse frequency of 6 Hz and a fluence of 5 J/cm². Zircon GJ-1 (599.8 ± 4.5 Ma; Jackson et al., 2004 [28]) and 91,500 (1062.4 ± 0.4 Ma; Wiedenbeck et al., 1995 [29]) served as primary and secondary reference materials, respectively. Typically, 20 s of a gas blank and 35–40 s of the signal interval were collected for data processing. Deep fractionation correction was carried out based on an exponential equation (Paton et al., 2010 [30]). NIST 610 was employed to calibrate the trace element content. The measured ages of the reference materials in the batch were as follows: 91,500 (1061.5 ± 4.1 Ma, 2δ, MSWD = 0.55, n = 32), GJ-1 (600.5 ± 2.9 Ma, 2δ, MSWD = 0.95, n = 32), showing consistency with the reference values within a specific uncertainty range. The zircon Plesovice was dated as “unknown samples” and yielded a weighted mean ²⁰⁶Pb/²³⁸U age of 336.1 ± 1.1 Ma (2δ, MSWD = 0.43, n = 32), aligning closely with the reference value within a defined uncertainty (337.13 ± 0.37 Ma; Sláma et al., 2008 [31]). The analysis results were processed using ICPMSDataCal 10.9 software (Liu et al., 2010 [32]). The concordia plots and weighted average U-Pb ages were determined using the IsoplotR 3.3 online program [33].

3.2.3. Zircon Hf Isotope Analysis

An in situ zircon Hf isotope analysis was conducted utilizing a RESOlution SE 193 laser ablation system coupled with a Thermo Fisher Scientific Neptune Plus MC-ICP-MS at Beijing Createch Testing Technology Co., Ltd., Beijing, China. The instrumental parameters and data acquisition methodologies were detailed by Hou et al. (2009) [34]. A stationary spot with a beam diameter of approximately 55 μm was employed. Helium served as the carrier gas to transport the ablated sample aerosol, mixed with argon from the laser ablation cell, to the MC-ICP-MS torch through a mixing chamber. The $^{176}\text{Lu}/^{175}\text{Lu} = 0.02658$ and $^{176}\text{Yb}/^{173}\text{Yb} = 0.796218$ ratios were determined to correct for the isobaric interferences of ^{176}Lu and ^{176}Yb on ^{176}Hf . For instrumental mass bias correction, the Yb isotope ratios were normalized to $^{172}\text{Yb}/^{173}\text{Yb} = 1.35274$ and the Hf isotope ratios to $^{179}\text{Hf}/^{177}\text{Hf} = 0.7325$ using an exponential law. It was assumed that the mass bias behavior of Lu followed that of Yb. The mass bias correction protocol was outlined by Hou et al. (2009) [34]. The zircon international standard GJ-1 was utilized as the reference standard. The measured $^{176}\text{Hf}/^{177}\text{Hf}$ ratios of the standard zircon GJ-1 were 0.282001 ± 33 (2δ , $n = 37$), which closely resembled the recommended $^{176}\text{Hf}/^{177}\text{Hf}$ ratio of 0.282003 ± 18 [35].

4. Results of Zircon Isotope Dating

The zircons separated from two types of gneiss in the ore-bearing wall rocks of the Hongtoushan “rhythmic member” exhibit three major groups in CL images. However, due to complex deformation and metamorphism, we will also utilize the contents of U and Th, as well as the Th/U ratio, to collectively constrain the genesis of the zircons. One main group of zircons is prismatic or fragmented crystals with length/width ratios of 3:1 to 5:1; these display relatively blurred oscillatory or sector zones. The second group of zircons have short prismatic or nearly rounded crystals with length/width ratios of 1:1 to 1.5:1, and the third group of zircons have different widths of core–rim structures that are characterized by clear oscillatory zoned cores surrounded by dark rims. Some grains even have clear corrosion rims. The analyzed data of the Hf isotopic and U-Pb dating are listed in Table A1. Detailed descriptions will be provided for each sample of the two types of gneiss.

4.1. Amphibole Plagioclase Gneiss

4.1.1. Sample HTS-1605-2

The zircon grains extracted from sample HTS-1605-2 are characterized by prismatic crystals with length-to-width ratios ranging from 3:1 to 5:1. In the CL images, the zircons are gray in color, and most of them exhibit blurred oscillatory zoning with a wide range of Th and U content (Th = 17.00–267.00 ppm; U = 80.30–373.00 ppm) and higher Th/U ratios, ranging from 0.11 to 1.08 (Figure 5A,B). This part of the zircons shows affinity with a magmatic origin [36]. A total of 15 U-Pb dating analyses were performed on this part of the zircons; the samples yielded a concordant age of 2510.5 ± 3.9 Ma ($N = 17$; MSWD = 2.1), which is consistent with the weighted mean age of 2512.1 ± 3.9 Ma ($N = 17/17$; MSWD = 3.4; see Figure 5C). At the same time, another few zircons display gray cores with a light, narrow corrosion field and unstructured dark rims in the CL images. Three analyses of the rims were performed; they exhibit low Th/U ratios ranging from 0.02 to 0.09 (Th = 3.66–26.80 ppm; U = 97–197 ppm) (Figure 5A,B), and have a $^{207}\text{Pb}/^{206}\text{Pb}$ mean age of 2472 ± 20 Ma. We consider that the rocks erupted at 2510.5 ± 3.9 Ma and were modified by a metamorphic event at 2472 ± 20 Ma.

4.1.2. Sample HTS-1605-6

Most zircons found in sample HTS-1605-6 are characterized by prismatic or fragmented crystals with length-to-width ratios ranging from 1:1 to 3:1. They are gray in color, exhibit blurred oscillatory or sector zoning in the CL images and have relatively higher contents and concentrated ranges of Th and U (Th = 76.78–219.04 ppm; U = 261.33–1118.18 ppm). The Th/U ratios range from 0.115 to 0.542 (see Figure 6A,B). These zircon signatures

indicate a magmatic origin [36]. A total of 13 U-Pb datings were conducted on sample HTS-1605-6, and these yielded an upper intercept age of 2528.8 ± 6.4 Ma ($N = 13$; MSWD = 0.56). The age is consistent with a weighted mean age of 2514.4 ± 4.0 Ma ($N = 13$; MSWD = 2.6), which is indicative of the formation age (see Figure 6C).

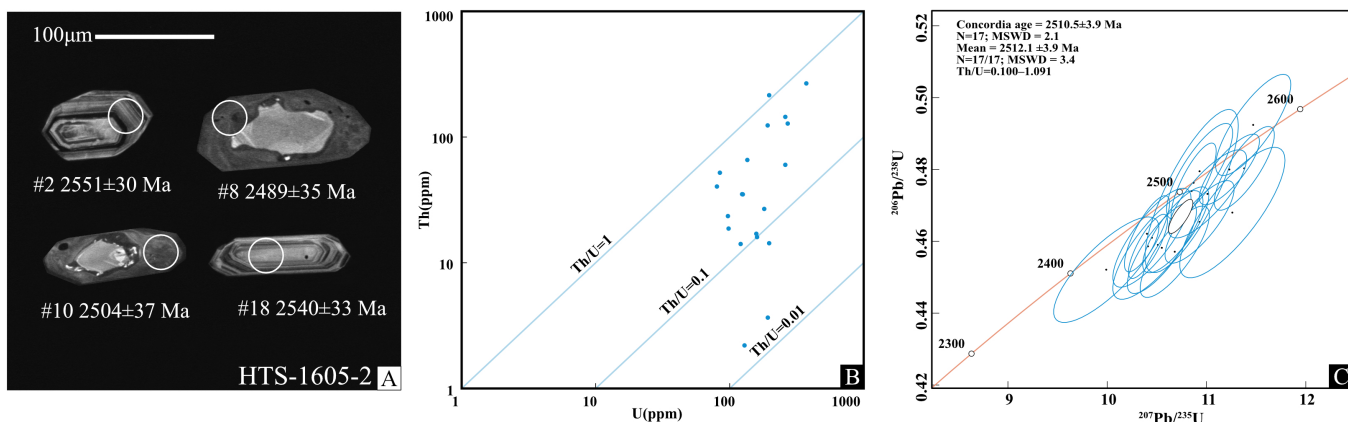


Figure 5. (A) CL images of the representative zircons; (B) Th and U concentration diagrams; (C) U-Pb zircon concordia diagrams for the HTS-1605-2 sample.

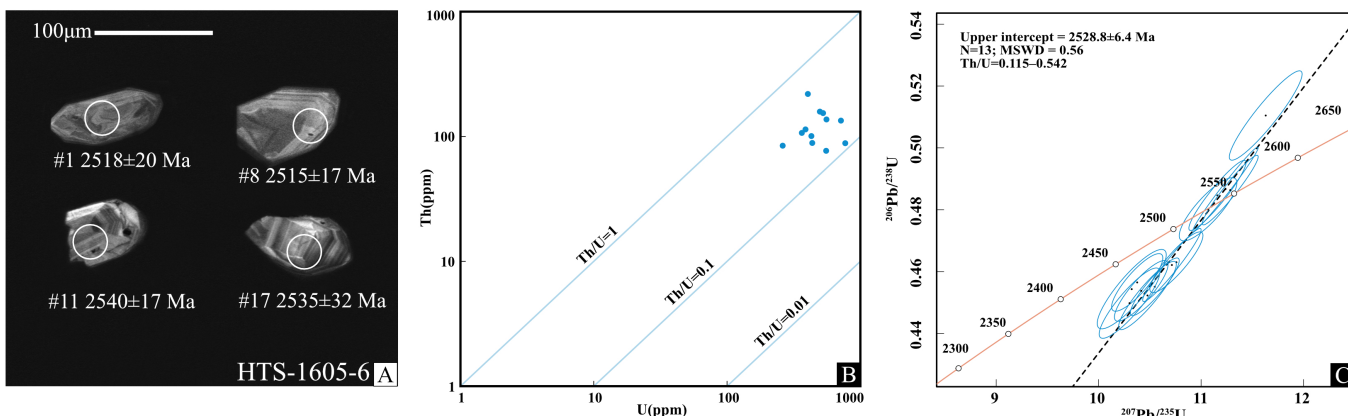


Figure 6. (A) CL images of the representative zircons; (B) Th and U concentration diagrams; (C) U-Pb zircon concordia diagrams for sample HTS-1605-6.

4.1.3. Sample HTS-1605-9

Similar to sample HTS-1605-2, most of the zircon grains in sample HTS-1605-9 exhibit prismatic crystals with length-to-width ratios of 2:1 to 5:1. Most of the zircons display core-rim structures, with a wide range in content regarding Th and U (Th = 11.30–978.00 ppm; U = 36.10–1039.00 ppm); they have Th/U ratios ranging from 0.123 to 0.941. A total of 15 points yield an upper intercept age of 2593 ± 11 Ma ($N = 15$; MSWD = 2.5, see Figure 7C), which can be considered as the formation age of HTS-1605-2. In contrast, few of them have relatively gray cores with blurred, irregular banded zoning rims in the CL images and have lower Th and U contents (Th = 6.35–26.00 ppm; U = 125.40–430.00 ppm), with Th/U ratios that are conspicuously lower than the ratios in the cores, ranging from 0.044 to 0.066 (see Figure 7A,B). These zircon signatures indicate the recrystallization of metamorphism. A total of four analyzed samples were obtained from the zircon rims. They have a $^{207}\text{Pb}/^{206}\text{Pb}$ age range from 2529 ± 23 to 2497 ± 23 Ma and yield an upper intercept age of 2526 ± 13 Ma ($N = 4$; MSWD = 0.19), which can be considered the metasomatism age.

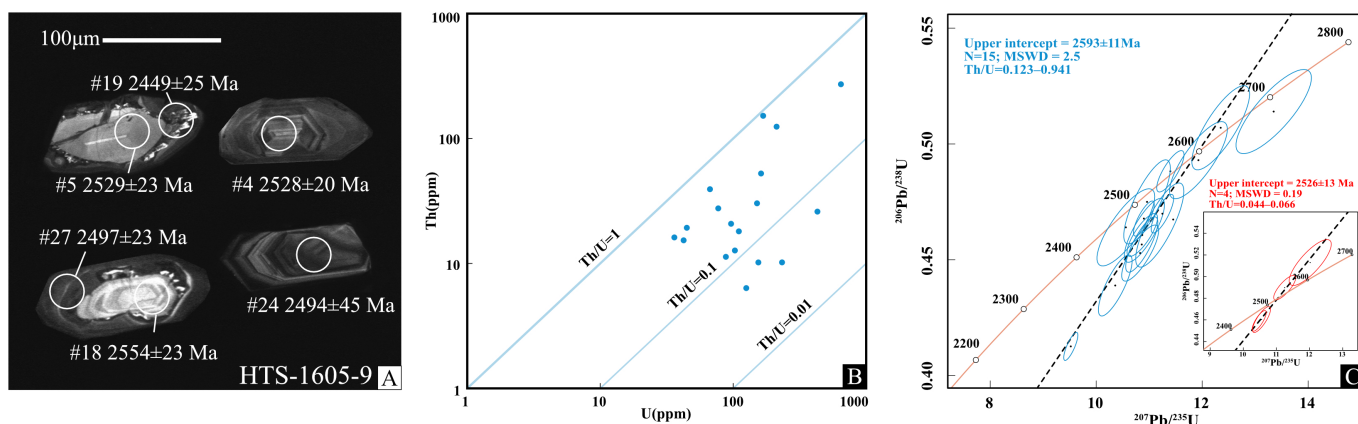


Figure 7. (A) CL images of the representative zircons; (B) Th and U concentration diagrams; (C) U-Pb zircon concordia diagrams for sample HTS-1605-9.

4.2. Biotite Plagioclase Gneiss

4.2.1. Sample HTS-1605-1

The zircons extracted from sample HTS-1605-1 display prismatic crystals with length-to-width ratios of 1:1.5 to 1:3. The zircon grains are round in shape with blurred sector zoning and most have extremely low contents and concentrated ranges of Th and U ($\text{Th} = 7.60\text{--}26.00 \text{ ppm}$; $\text{U} = 421.00\text{--}2060.00 \text{ ppm}$), and the Th/U ratios range from 0.012 to 0.040, which are indicative of their metamorphic origin (see Figure 8A,B). A total of 19 U-Pb dating analyses were performed on the zircon grains, and 16 points with low Th/U ratios yielded an upper intercept age of $2471.8 \pm 2.6 \text{ Ma}$ ($N = 16$; MSWD = 0.81) and corresponded to a weighted mean age of $2471.2 \pm 2.0 \text{ Ma}$ ($N = 16$; MSWD = 4.7), which is indicative of the recrystallization age (Figure 8C). Some individual zircons exhibit a core–rim structure, with a bright, small, and circular core surrounded by a darker rim. Due to the small size of the cores, we only tested three zircons. Their cores have higher Th/U ratios ranging from 0.216 to 0.438, indicating that the cores are of magmatic origin. Three core points have a $^{207}\text{Pb}/^{206}\text{Pb}$ age range of 2481 ± 23 to $2466 \pm 21 \text{ Ma}$.

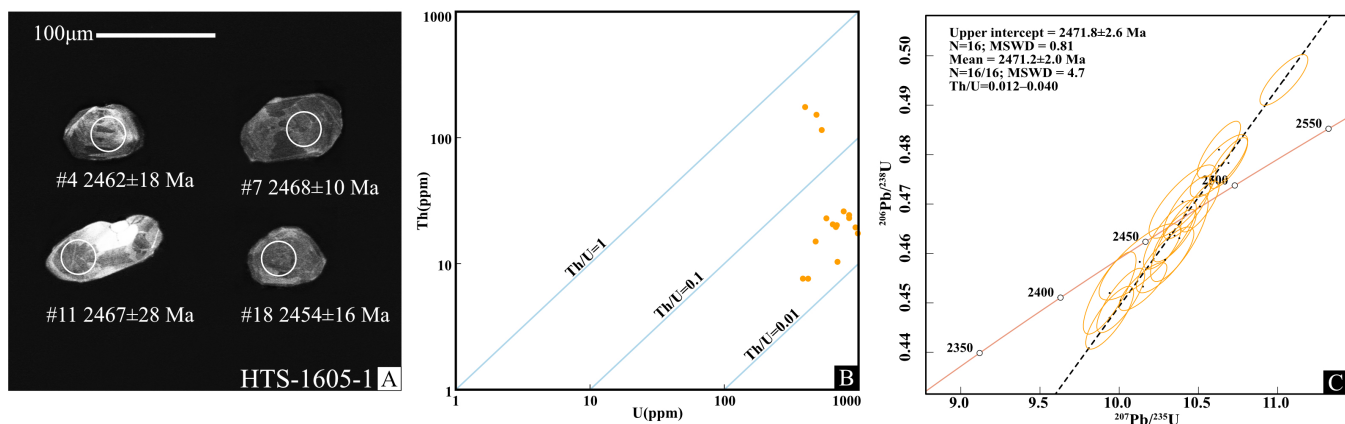


Figure 8. (A) CL images of the representative zircons; (B) Th and U concentration diagrams; (C) U-Pb zircon concordia diagrams for sample HTS-1605-1.

4.2.2. Sample HTS-1605-3

The zircons obtained from sample HTS-1605-3 display prismatic crystals with length-to-width ratios of 1:1.5 to 1:3. The zircon grains generally display relatively bright cores and dark rims. Most of the zircon grains are small in size, with extremely low Th/U ratios ranging from 0.005 to 0.057 ($\text{Th} = 2.28\text{--}48.23 \text{ ppm}$; $\text{U} = 391.94\text{--}1200.00 \text{ ppm}$). After comparing the Th/U ratios between the cores and rims, combined with the uniformly positive $\epsilon\text{Hf}(t)$ and relatively concentrated ages, we consider that the zircon grains in HTS-1605-3 are more

likely to be inherited zircons, and the low Th/U ratios could be attributed to the influence of late-stage hydrothermal fluids [37] (see Figure 9A,B). A total of 15 analyses yielded an upper intercept age of 2509.0 ± 5.8 Ma (N = 15; MSWD = 0.25), which is consistent with the weighted mean age of 2503.3 ± 2.8 Ma (N = 15; MSWD = 0.91) (see Figure 9C). The results approximately represent the formation age of biotite plagioclase gneiss.

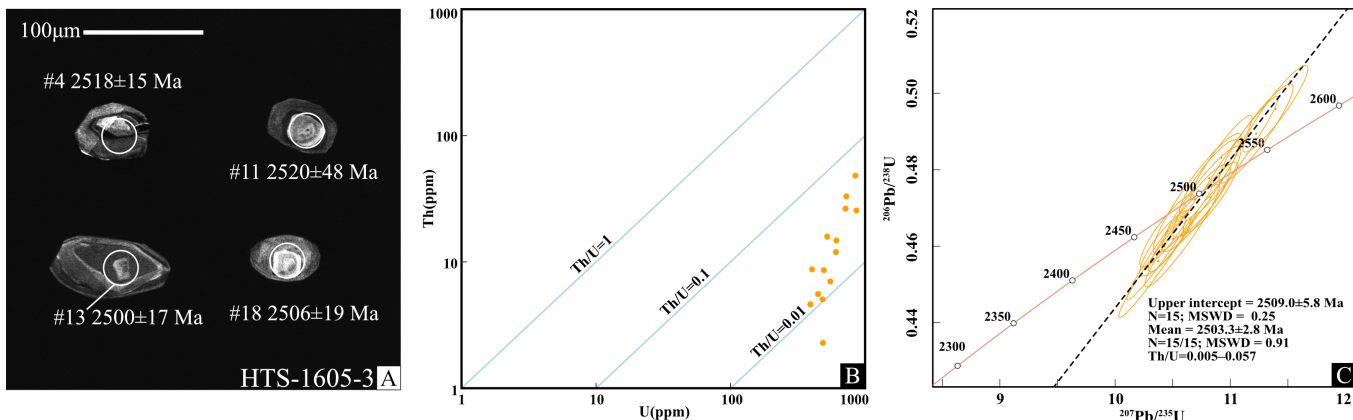


Figure 9. (A) CL images of the representative zircons; (B) Th and U concentration diagrams; (C) U-Pb zircon concordia diagrams for sample HTS-1605-3.

4.2.3. Sample HTS-1605-8

Most zircons obtained from sample HTS-1605-8 are mostly irregular crystals with length-to-width ratios of approximately 1:1.5 to 2:1, appearing light gray in the CL images, with faint zoning patterns observed internally. A few zircons have small, bright residual cores. These characteristics indicate that they were more likely formed by recrystallization (Figure 10A). However, due to the small size of the residual cores, they were not suitable for testing. Therefore, all the tests were conducted on homogeneous zircon grains. They have Th and U contents of Th = 21.20–333.20 ppm and U = 56.00–844.00 ppm and Th/U ratios ranging from 0.108 to 1.169. A total of 28 U-Pb dating analyses yielded a concordia age of 2468.5 ± 2.4 Ma (N = 28; MSWD = 1.2), and this corresponds with the mean age of 2469.0 ± 2.4 Ma (N = 28/28; MSWD = 1.5), which may indicate the recrystallization age of the zircons (Figure 10C).

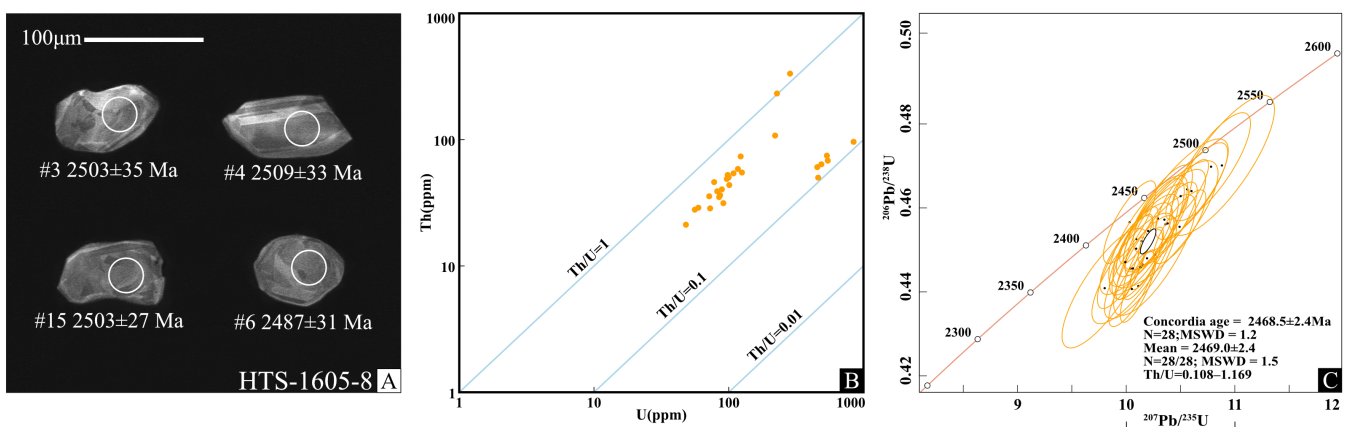


Figure 10. (A) CL images of the representative zircons; (B) Th and U concentration diagrams; (C) U-Pb zircon concordia diagrams for sample HTS-1605-8.

5. Results of Hf Isotopic Analysis

The Lu-Hf data on the zircons from the individual samples are briefly listed in Table 1. A total of 40 of the Lu-Hf isotopes analyzed were obtained from the zircon grains from amphibole plagioclase gneiss. The results are presented in Table A2. The results of the am-

phibole plagioclase gneiss samples show the initial $^{176}\text{Hf}/^{177}\text{Hf}$ ratios range from 0.28128 to 0.28144. The $\epsilon\text{Hf(t)}$ values are in the range of 3.91 to 10.45. The TDM1 ages are between 2687.69 Ma and 2453.51 Ma, and the TDM2 ages range from 2776.75 to 2411.13 Ma. Meanwhile, 48 Lu-Hf isotope analyses were performed on the zircon grains from biotite plagioclase gneiss. The results of biotite plagioclase gneiss samples show the initial $^{176}\text{Hf}/^{177}\text{Hf}$ ratios range from 0.28126 to 0.28143. The $\epsilon\text{Hf(t)}$ values are in the range of 3.07 to 9.16. The TDM1 ages are between 2728.02 Ma and 2489.84 Ma, and the TDM2 ages range from 2838.15 to 2469.98 Ma.

Table 1. Summary of Lu-Hf ages obtained in this study.

Sample	Lithology	Mineral	Size (μm)	Hf(I)	$\epsilon\text{Hf(t)}$	TDM1 (Ma)	TDM2 (Ma)
HTS-1605-2	Amphibole plagioclase gneiss	zircon	50–120 (avg: 60–75)	0.28128–0.28144	3.91–10.45	2453.51–2619.01	2411.13–2715.70
HTS-1605-6	Amphibole plagioclase gneiss	zircon	45–110 (avg: 70–80)	0.28128–0.28139	4.30–8.45	2557.09–2687.69	2572.63–2776.15
HTS-1605-9	Amphibole plagioclase gneiss	zircon	70–150 (avg: 100–105)	0.28131–0.28137	4.85–6.60	2568.22–2634.44	2607.11–2711.56
HTS-1605-1	Biotite plagioclase gneiss	zircon	60–90 (avg: 70–80)	0.28130–0.28137	3.36–6.14	2558.37–2658.42	2615.79–2781.03
HTS-1605-3	Biotite plagioclase gneiss	zircon	40–110 (avg: 80–90)	0.28126–0.28143	3.07–9.16	2489.97–2728.02	2469.98–2838.15
HTS-1605-8	Biotite plagioclase gneiss	zircon	50–80 (avg: 60–70)	0.28136–0.28142	6.51–8.55	2498.84–2578.64	2494.38–2621.70

Note: Age (Ma) is the weighted mean $^{207}\text{Pb}/^{206}\text{Pb}$ age; errors are δ ; n is the number of analyses. For the complete data, see Table A2.

6. Geochemical Result of Ore-Bearing Metamorphic Rocks

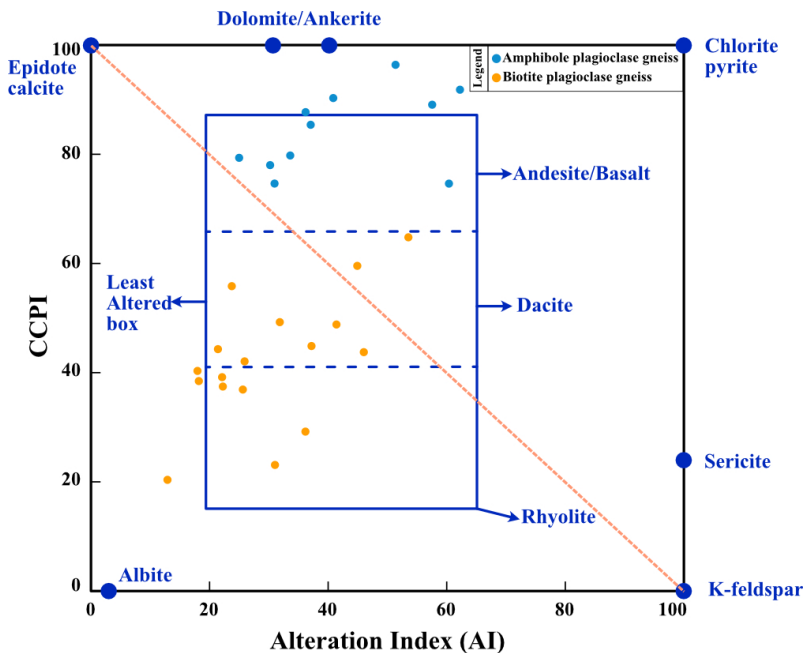
6.1. Assessing Element Mobility

The Archean Hongtoushan VMS deposit has undergone amphibolite-to-granulite facies metamorphism and multi-period tectonic deformation [22]; it is necessary to evaluate the impact of high-grade metamorphism on element mobility, which may alter the geochemical properties of host rocks.

Altered samples generally have an LOI (enrichment in loss on ignition) of >6 wt% or $\delta\text{Ce} < 0.9$ or >1.1 [38]. Moreover, the “alteration box plot” (Figure 11) from Large et al. (2001) [39] is also used to assess element mobility. In the CCPI versus AI diagram, the samples plotted in the least altered box are considered unaffected by hydrothermal alteration. After removing the obviously altered samples, 20 samples were identified for further discussion (Table A3). Previous studies have demonstrated that Zr is one of the most stable elements [38,40] and is appropriate for assessing element mobility. By comparing Zr diagrams with other select elements, good correlations among Zr and HFSEs and transition elements are observed (Figure 12I–L). These elements will be further discussed in terms of petrogenesis, magma signatures, and tectonic settings.

6.2. Major Element Composition

The major element composition of the ore-bearing metamorphic rocks is summarized in Table A3. The results show that the ore-bearing metamorphic rocks have a continuous oxide content. The biotite plagioclase gneiss samples have the following chemical compositions: SiO_2 ranging from 64.64 to 84.42 wt%, $\text{Fe}_2\text{O}_3\text{T}$ ranging from 1.64 to 7.67 wt%, TiO_2 ranging from 0.10 to 0.61 wt%, MgO ranging from 0.33 to 4.79 wt%, K_2O ranging from 0.74 to 3.59 wt%, CaO ranging from 0.77 to 4.84 wt%, Al_2O_3 ranging from 6.94 to 16.46 wt%, and Na_2O ranging from 1.93 to 5.85 wt% (see Table 2). In comparison, the amphibole plagioclase gneiss has lower values: SiO_2 ranging from 47.63 to 56.53 wt%, $\text{Fe}_2\text{O}_3\text{T}$ ranging from 8.75 to 13.21 wt%, TiO_2 ranging from 0.52 to 2.44 wt%, MgO ranging from 3.17 to 7.42 wt%, K_2O ranging from 0.34 to 2.97 wt%, and CaO ranging from 3.02 to 11.57 wt%, but it has a higher Na_2O content, ranging from 2.27 to 3.71 wt%, and Al_2O_3 content, ranging from 14.25 to 16.67 wt% (see Table 2). There is obviously a negative correlation between the content of selected oxides and the content of SiO_2 , except for the contents of Na_2O and K_2O (Figure 12A–H).



Equations:
 $\text{CCPI} = \text{Chlorite-Carbonate-Pyrite Index}$
 $\text{CCPI} = 100(\text{MgO} + \text{FeO}) / (\text{MgO} + \text{FeO} + \text{Na}_2\text{O} + \text{K}_2\text{O})$
 $\text{AI} = \text{Alteration Index}$
 $\text{AI} = 100(\text{K}_2\text{O} + \text{MgO}) / (\text{K}_2\text{O} + \text{MgO} + \text{Na}_2\text{O} + \text{CaO})$
 FeO is total $(\text{FeO} + \text{Fe}_2\text{O}_3)$ content of the rock

Figure 11. CCPI versus AI alteration box plot (Large et al. (2001) [39]).

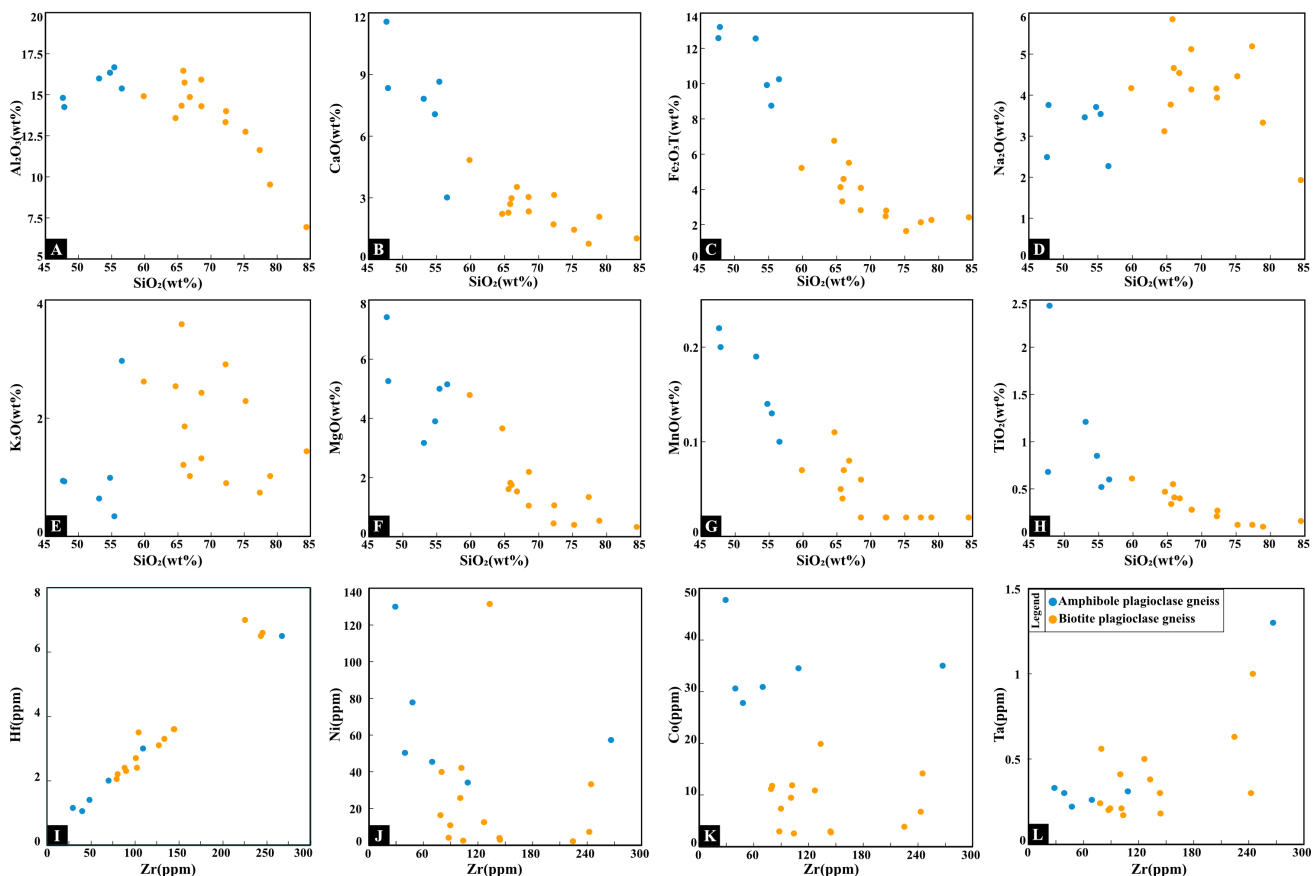


Figure 12. (A–H) Major (wt%) elements versus SiO_2 (wt%) diagrams and (I–L) Zirconium (ppm) versus typical elements (ppm) diagrams of the ore-bearing host rocks in Hongtoushan.

Table 2. Major (wt%) and trace (rare earth) element composition and the relevant parameter ranges of the host rocks of the Hongtoushan VMS deposit.

Rock Type		Amphibole Plagioclase Gneiss														
Value		Al ₂ O ₃	BaO	CaO	Cr ₂ O ₃	Fe ₂ O ₃ T	K ₂ O	MgO	MnO	Na ₂ O	P ₂ O ₅	SiO ₂	SrO	TiO ₂	LOI	Total
Max		16.67	0.04	11.57	0.06	13.21	2.97	7.42	0.22	3.71	0.34	56.53	0.04	2.44	3.19	99.90
Min		14.25	0.02	3.02	<0.01	8.75	0.34	3.17	0.10	2.27	0.05	47.63	<0.01	0.52	0.72	99.60
Avg		15.57	0.03	7.75	0.03	11.21	1.14	4.98	0.16	3.21	0.18	52.54	0.02	1.05	1.96	99.82
Value		La	Ce	Pr	Nd	Sm	Eu	Gd	Tb	Dy	Ho	Er	Tm	Yb	Lu	Co
Max		28.30	65.80	9.22	39.40	8.81	2.66	8.65	1.28	7.06	1.45	3.69	0.50	3.21	0.46	47.70
Min		6.50	14.50	1.89	8.00	1.94	0.58	1.99	0.35	2.06	0.41	1.15	0.18	1.06	0.16	27.80
Avg		12.07	28.78	3.99	17.33	4.20	1.17	4.19	0.68	3.98	0.83	2.32	0.34	2.21	0.33	34.42
Value		Ni	Cu	Zr	Sr	Y	Zn	Cs	Ba	Pb	U	V	Cr	Rb	Ga	Hf
Max		130.00	67.10	267.00	374.00	36.40	366.00	4.93	277.00	35.90	0.40	245.00	203.00	105.25	25.30	6.50
Min		34.10	10.90	29.15	118.50	9.70	77.00	0.20	59.30	1.70	0.13	103.00	20.00	3.55	16.20	1.05
Avg		65.82	37.65	93.81	220.33	21.38	171.50	1.11	162.22	8.93	0.24	194.17	110.17	35.29	19.33	2.52
Value		Ta	Th	Nb	P	Ti	K	ΣREE	ΣLREE	ΣHREE	δEu	δCe	(La:Sm) _N	(La:Yb) _N	(Sm:Nd) _N	(Gd:Yb) _N
Max		1.30	3.76	21.20	1490.00	14,627.80	24,654.86	180.49	154.19	15.04	1.05	1.05	3.06	7.12	0.89	2.17
Min		0.22	0.48	3.35	220.00	3117.40	2822.44	41.78	33.81	7.51	0.62	0.96	1.14	1.51	0.68	1.16
Avg		0.45	1.38	7.60	800.00	6294.75	9421.98	82.42	67.54	14.88	0.84	1.00	1.88	3.91	0.77	1.48
Rock Type		Biotite Plagioclase Gneiss														
Value		Al ₂ O ₃	BaO	CaO	Cr ₂ O ₃	Fe ₂ O ₃ T	K ₂ O	MgO	MnO	Na ₂ O	P ₂ O ₅	SiO ₂	SrO	TiO ₂	LOI	Total
Max		16.46	0.11	4.84	0.04	6.76	3.59	4.79	0.11	5.85	0.25	84.42	0.08	0.61	3.90	100.10
Min		6.94	0.01	0.77	<0.01	1.64	0.74	0.33	0.02	1.93	0.02	64.64	<0.01	0.10	0.63	99.03
Avg		13.45	0.07	2.44	0.02	3.59	1.85	1.61	0.04	4.17	0.11	70.44	0.04	0.31	1.67	99.78
Value		La	Ce	Pr	Nd	Sm	Eu	Gd	Tb	Dy	Ho	Er	Tm	Yb	Lu	Co
Max		37.90	78.70	9.82	38.80	9.02	1.45	9.85	1.75	10.55	2.36	6.85	0.99	6.58	0.96	19.90
Min		3.60	6.80	0.75	2.80	0.72	0.30	0.50	0.06	0.26	0.05	0.13	0.02	0.16	0.02	2.60
Avg		20.32	40.00	4.48	16.51	3.17	0.75	2.82	0.46	2.54	0.53	1.47	0.22	1.43	0.23	8.49
Value		Ni	Cu	Zr	Sr	Y	Zn	Cs	Ba	Pb	U	V	Cr	Rb	Ga	Hf
Max		131.50	80.40	245.00	723.00	67.40	585.00	7.32	2810.00	34.30	3.30	94.00	196.00	109.25	20.90	7.00
Min		2.10	2.90	80.15	47.30	1.35	22.00	0.48	78.70	3.20	0.16	9.00	20.00	14.10	8.56	2.20
Avg		23.89	21.36	136.11	306.61	12.19	103.43	1.79	587.39	10.91	0.78	43.14	66.57	51.28	15.94	3.66
Value		Ta	Th	Nb	P	Ti	K	ΣREE	ΣLREE	ΣHREE	δEu	δCe	(La:Sm) _N	(La:Yb) _N	(Sm:Nd) _N	(Gd:Yb) _N
Max		1.00	15.90	12.10	1120.00	3656.95	29,801.67	211.95	172.06	39.89	2.53	1.02	7.86	60.68	0.79	5.71
Min		0.17	0.33	2.90	100.00	599.50	6142.96	17.71	15.25	1.20	0.39	0.90	2.41	3.25	0.40	0.82
Avg		0.38	5.22	5.42	500.00	1849.89	15,351.48	94.93	85.23	9.69	1.05	0.96	4.61	20.56	0.59	2.46

6.3. Trace and Rare Earth Elements

Based on the data from the ore-bearing host rocks from the Hongtoushan VMS deposit, transition metal elements, such as Co (27.80–47.70 ppm; avg: 34.42 ppm), Ni (34.10–131.50 ppm; avg: 65.82 ppm), Cu (10.90–67.10 ppm; avg: 37.65 ppm), and Zn (77.00–366.00 ppm; avg: 171.50 ppm), are relatively slightly more concentrated in amphibole plagioclase gneiss than in biotite plagioclase gneiss, which exhibits Co, Ni, Cu, and Zn concentrations of 2.60–19.90 ppm (avg: 8.49 ppm), 2.10–131.50 ppm (avg: 23.89 ppm), 2.90–80.40 ppm (avg: 21.36 ppm), and 22.00–585.00 ppm (avg: 103.43 ppm), respectively. On the other hand, the biotite plagioclase gneiss is relatively enriched in LILEs (large-ion lithophile elements): (K: 6142.96–29,801.67 ppm, avg: 15,351.48 ppm; Rb: 14.1–109.25 ppm, avg: 51.28 ppm; Sr: 47.30–723.00 ppm, avg: 306.61 ppm; Ba: 78.70–2810.00 ppm, avg: 5878.39 ppm).

In the chondrite-normalized REE pattern diagram for the amphibole plagioclase gneiss, the samples display near flat to weakly LREE-enriched REE patterns, with a mean La/Yb_N value of 3.91, and weakly negative δEu anomalies, with a mean δEu value of 0.84 (Figure 13B). In the primitive mantle-normalized spider diagram for the amphibole plagioclase gneiss, the samples exhibit weak negative anomalies in Ta, Nb, and Ti and very weak to medium negative Zr-Hf anomalies (Figure 13A). In contrast, the biotite plagioclase gneiss in the chondrite-normalized REE pattern diagram exhibits remarkable

LREE-enriched patterns, with a wide range of La/Yb_N from 3.25 to 60.68, and they have a δEu value range from 0.39 to 2.53 (Figure 13D). In the spider diagram, the samples show more prominent negative Ta, Nb, Ti, and P anomalies and positive Zr-Hf anomalies (Figure 13C). Notably, no Ce anomalies are observed in any of the host rocks, with mean δCe values of 1.00 and 0.96 for amphibole plagioclase gneiss and biotite plagioclase gneiss, respectively (see Table 2).

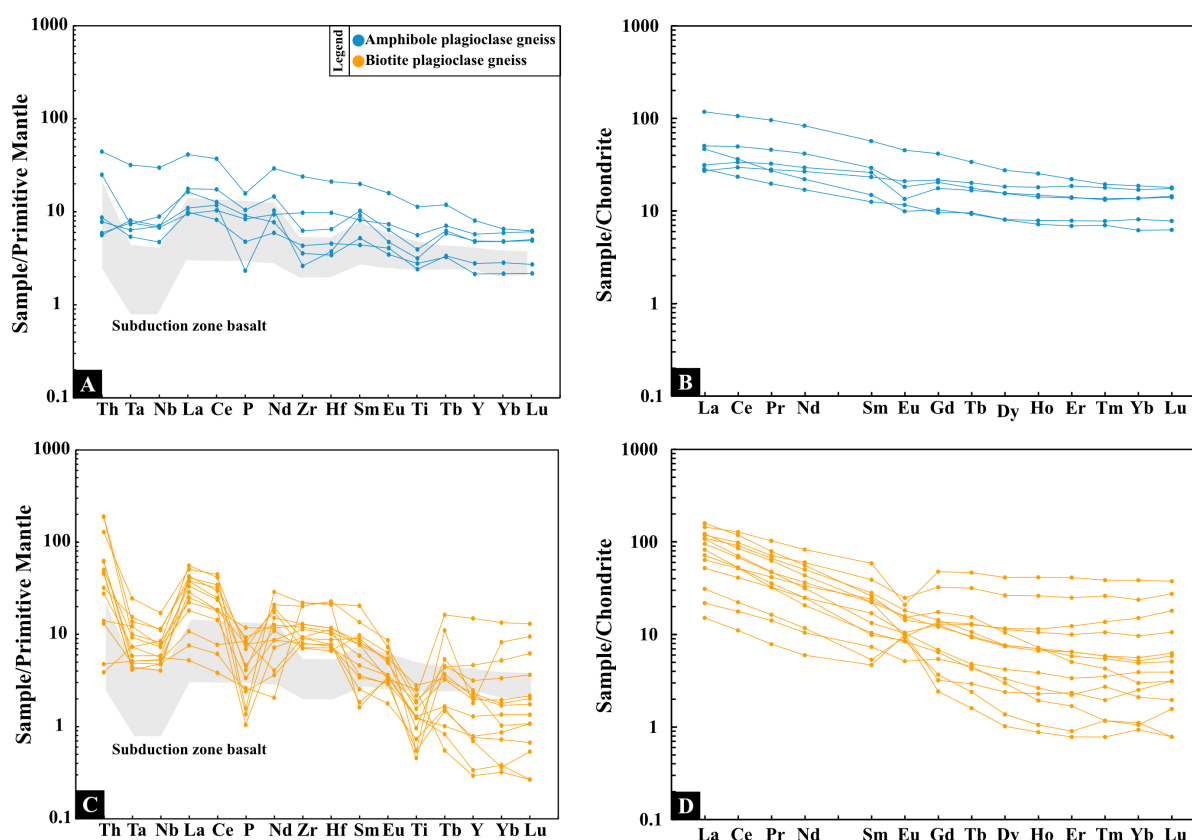


Figure 13. Primitive mantle-normalized trace element spider and chondrite-normalized REE pattern diagrams of rocks (A–D) (normalizing values from Sun and McDonough [41]).

7. Discussion

7.1. Petrogenesis of Hongtoushan Ore-Bearing Rocks

Ga versus Zr/TiO_2 and Nb/Y versus TiO_2 diagrams are used to classify metamorphic rocks in the Hongtoushan VMS deposit. In the Ga versus Zr/TiO_2 diagram, the amphibole plagioclase gneiss samples are mostly plotted in the basalt field, while the biotite plagioclase gneiss samples are plotted in the andesite to rhyolite field (Figure 14A). In the Nb/Y versus Zr/TiO_2 diagram, the amphibole plagioclase gneiss samples are mostly plotted in the basalt and andesite/basalt field, while the biotite plagioclase gneiss samples are placed in the andesite, rhyodacite, rhyolite, and trachyandesite field (Figure 14B). Meanwhile, the compositions of metamorphic rocks show a continuous variation trend for the major element versus SiO_2 diagrams (Figure 12). According to this study, and when combined with previous research [22], the amphibole plagioclase gneiss has a protolith of basalt, while the biotite plagioclase gneiss has protoliths of andesite and rhyolite. It is believed that the studied area has experienced a complete volcanic cycle from basic volcanic rocks to medium-acidic volcanic rocks.

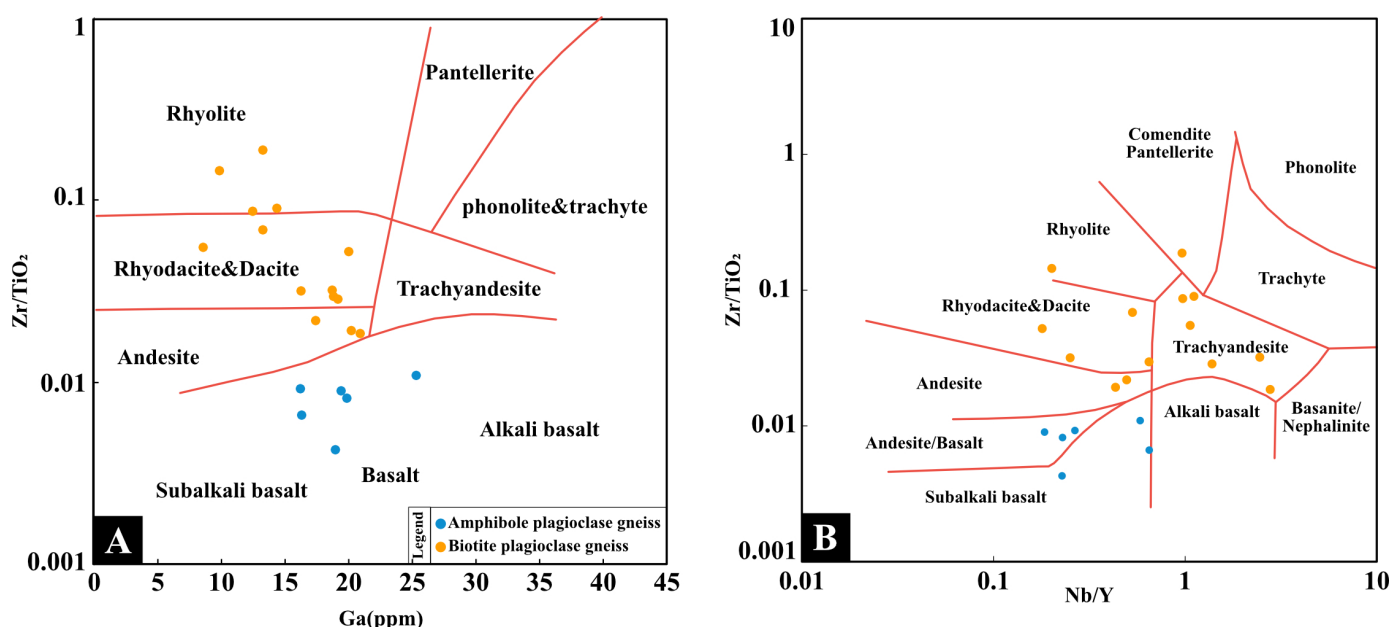


Figure 14. (A) Diagram of Ga (ppm) versus Zr/TiO₂ for metamorphic rocks from the Hongtoushan VMS deposit. (B) Diagram of Nb/Y versus Zr/TiO₂ for metamorphic rocks from the Hongtoushan VMS deposit ((A,B) are both from Winchester and Floyd, 1997 [42]).

7.1.1. Crustal Contamination and Fractional Crystallization

It is essential to note that the composition of any given magma can be influenced by various factors, such as the mantle source's composition, melting degree, fractionation, and, especially, crustal contamination. The magma can become enriched in elements such as Zr, Hf, and LREEs while being depleted in Nb and Ta under significant crustal contamination [43–51]. This may result in a signature depleted in Nb, Ta, and Ti, similar to that observed in subduction-related magmatism, which is referred to as a “fake subduction signal” by Ernst (2005) [52]. Thus, it is imperative to conduct a more comprehensive assessment of the potential factors that could potentially exert an influence on the constituent composition of the magma.

Previous protolith recovery results indicate that the protolith of amphibole plagioclase gneiss is a series of basalt. However, the amphibole plagioclase gneiss of the Hongtoushan VMS deposit displays weakly enriched LREE patterns with weakly negative Nb, Ta, and Ti anomalies and insignificant- to medium-negative Zr and Hf anomalies (Figure 13A,B). In the Th/Yb versus Nb/Yb diagram (Figure 15A), the amphibole plagioclase gneiss samples are concentrated around E-MORB and SCLM end-members within the mantle array (the field between the dashed lines) and show a remarkable trend to the vector of fractional crystallization and an insignificant trend of crustal contamination. In the Th/Nb versus La/Sm diagram (Figure 15B), all samples except one have extremely high Th/Nb ratios, which may have been significantly affected by crustal contamination. The rest of the samples are mainly plotted near the primitive area and display a weak trend toward upper-crust fractional crystallization. Therefore, it can be presumed that the amphibole plagioclase gneiss suffered limited crustal contamination.

7.1.2. Amphibole Plagioclase Gneiss

The previous results suggest that the amphibole plagioclase gneiss has undergone slight crustal contamination. Thus, the weak enrichment of LREE patterns and weak negative Nb, Ta, and Ti anomalies are unlikely to have been caused by crustal contamination completely. These characteristics are more likely inherited from enriched mantle sources. In the Nb/Yb versus Th/Yb diagram, the amphibole plagioclase gneiss is mainly plotted in the field near the E-MORB end-member and shows a trend that is parallel with MORB-OIB, reflecting the mantle plume source [55]. The samples slightly falling above the array can be

interpreted by the limited crustal contamination mentioned above (Figure 16A). Likewise, in the Nb/Y versus Zr/Y diagram, the amphibole plagioclase gneiss is mainly plotted near the end-member of primitive mantle within the field of OPB (ocean plateau basalt) and displays a similar vector to the batch melting array (Figure 16B). This type of mantle melting means that the melt is in equilibrium with the mantle residue until it separates from it (segregates) and intrudes into the crust [57,58]. Therefore, based on the analytical results, we propose that amphibole plagioclase gneiss is more likely generated from the mantle plume head.

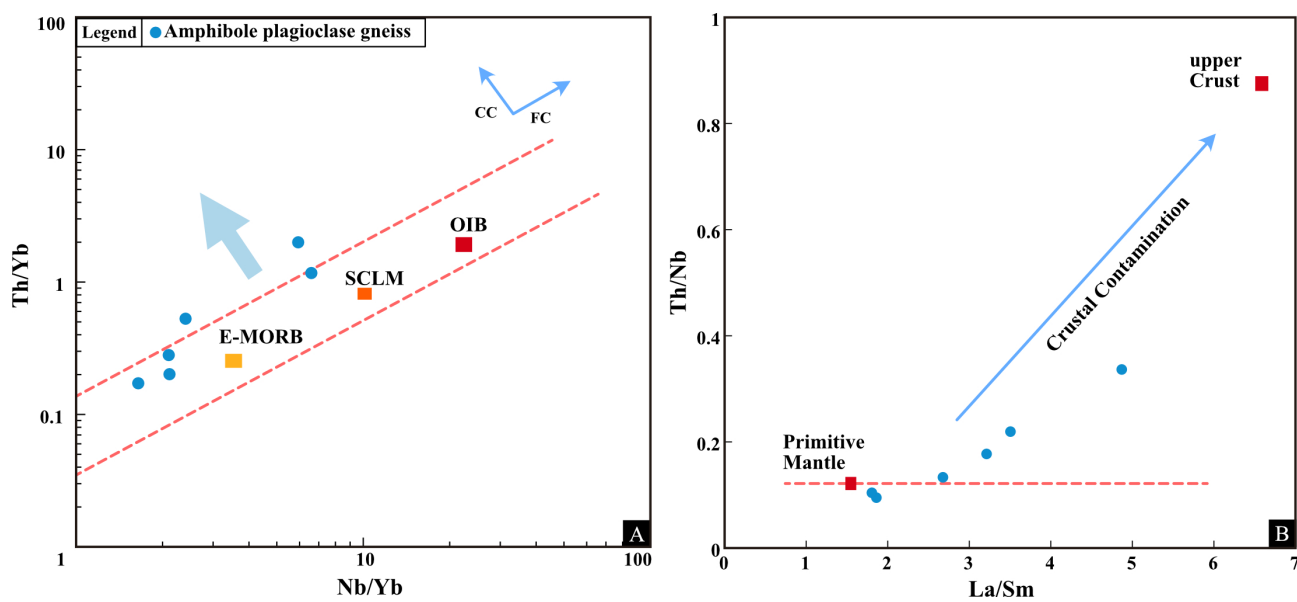


Figure 15. (A) Th/Yb versus Nb/Yb diagram of meta-host rocks from the Hongtoushan VMS deposit (modified from Hari et al. (2018) [53]). The N-MORB, E-MORB, and OIB (ocean island basalt) compositions are from Sun and McDonough (1989) [41]. The SCLM (sub-continental lithospheric mantle) composition is from McDonough (1990) [54]. Vectors CC and FC approximate the direction of crustal contamination and fractional crystallization, respectively. The dashed lines indicate the mantle array (Pearce 2008 [55]). (B) La/Sm versus Th/Nb diagram of Hongtoushan ore-bearing rocks (from Piercy et al. (2002) [56]).

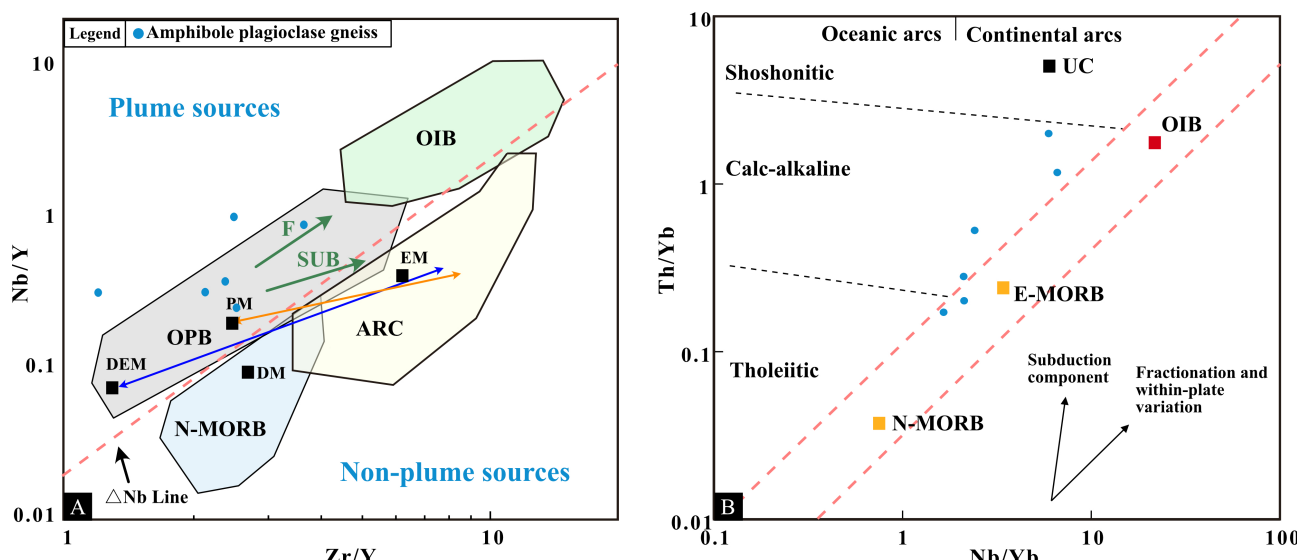


Figure 16. (A) Nb/Yb versus Th/Yb (modified from Pearce (2008 [55])); (B) Zr/Y versus Nb/Yb diagram modified by Condie et al. (2005) [57]. ARC = arc-related basalt; OPB = oceanic plateau basalt;

OIB = oceanic island basalt; N-MORB = normal ocean ridge basalt; F = batch melting; SUB = subduction; orange arrow: a plume mixing array for early Archean non-arc basalts; blue arrow: a plume mixing array for late Archean non-arc basalts.

7.1.3. Biotite Plagioclase Gneiss

Based on the REE patterns, Eu anomalies, Zr/Y ratios, and trace element abundances, Hart et al. (2004) [59] categorized felsic rocks in Archean terranes into four groups: FI to FIV. The FI group exhibits high Zr/Y ratios, low HFSE abundances, relatively steep REE patterns, and Eu anomalies ranging from weakly negative to moderately positive. In contrast, the FIII rhyolites may be subdivided into two types. FIIIA rhyolites exhibit variable negative Eu anomalies, low Zr/Y, and intermediate abundances of HFS elements. FIIIB rhyolites exhibit pronounced negative Eu anomalies, low Zr/Y, and high abundances of HFSEs. The FIV group contains rhyolites and high-silica rhyolites, which are characterized by flat to slightly LREE-depleted REE patterns and low REE and HFSE abundances. The biotite plagioclase gneiss of the Hongtoushan VMS deposit displays significant enrichment in LREEs (avg: $(\text{La}/\text{Yb})_N = 18.22$) and remarkable negative Ta, Nb, and Ti anomalies with relatively high Zr/Y ratios (3.64–75.59) (Figure 13C,D). In the $(\text{La}/\text{Yb})_N$ versus Yb_N diagram (Figure 17A), the biotite plagioclase gneiss of the Hongtoushan VMS deposit predominantly shows an affinity with FI-type and FII-type felsic volcanic rocks.

FII group rocks are generally considered to host few deposits. Researchers proposed that these rocks are generally interpreted as the products of lower-temperature melts ($<900^\circ\text{C}$) at deeper levels in the crust (>10 km). Due to the lower temperature and loss of heat during transport to the surface, they have less potential to drive the hydrothermal convection system for a long time [60,61]. However, Cathles et al. (1997) [62] and Barrie et al. (1999) [63] claim that the heat engines that drive ore forming should not be solely considered. Thermal models showed that the period of time that an intrusion is able to sustain high-temperature hydrothermal convection is primarily a function of the mass of the intrusion, the temperature of the magma, and the temperature and permeability of the host rocks. Larger, higher temperature mafics or ultramafic intrusions emplaced at deeper crustal levels (10–18 km), where the country rocks are characterized by a lower permeability and higher rock-wall temperatures, favor the generation of long-lived, high-temperature, convective hydrothermal systems (e.g., Cathles et al. (1997) [62]).

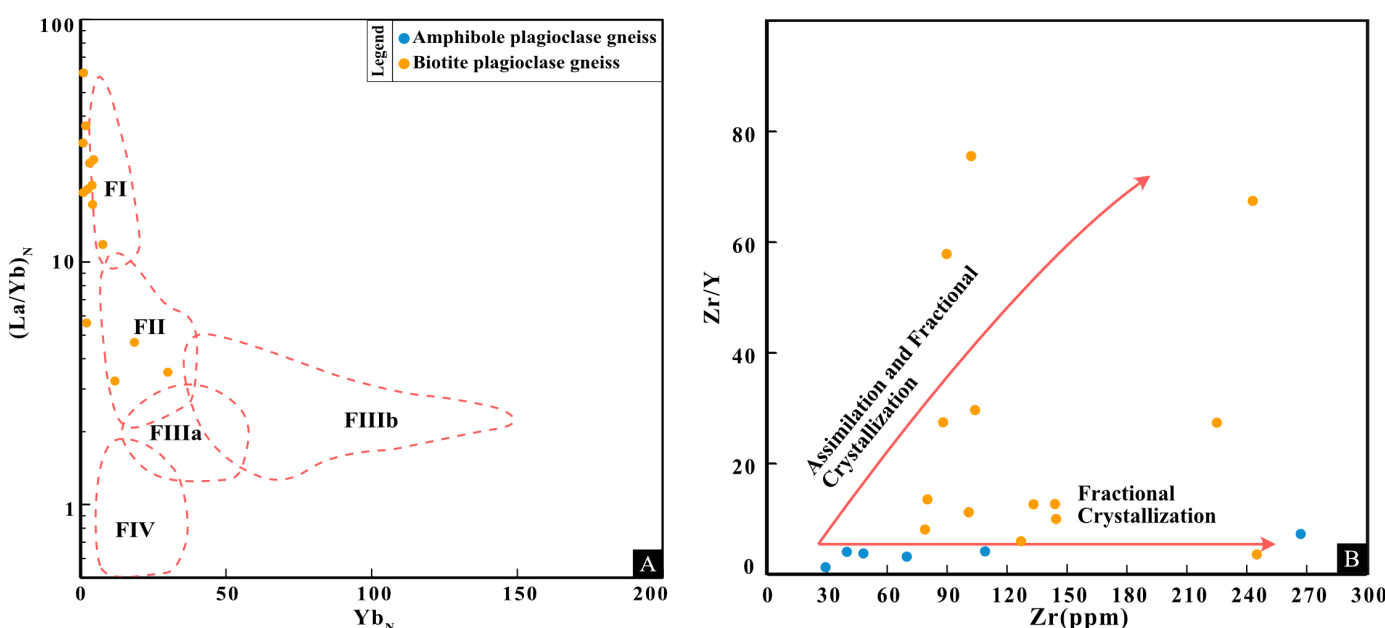


Figure 17. (A) $(\text{La}/\text{Yb})_N$ versus Yb_N diagram from Hart et al. (2004) [59]; (B) Zr/Y versus Zr diagram of the Hongtoushan VMS deposit (from Liu (2018) [64] and Rollinson, H. (1993) [65]).

In the previous discussion, we discovered that the parent magma of the amphibole plagioclase gneiss is formed by the partial melting of about 10%–30% garnet-spinel lherzolite. The tectonic setting is interpreted as a margin rift associated with mantle plume activity. A continuous magmatic evolution trend is shown by gradual changes in the basaltic to rhyolitic composition of the original volcanics (Figures 12 and 14A) and the stable fractional crystallization trend with limited crustal assimilation trends in the Zr/Y versus Zr diagram, which displays a commonly continuous magmatic evolution process. Therefore, the petrogenesis of biotite plagioclase gneiss can be more reasonably interpreted as crustal assimilation combined with the fractional crystallization of basic magma (the magma source of amphibole plagioclase gneiss) in the rift environment. The stretching environment provided by rift structures and the high-temperature heat source from the mantle plume activity create ideal conditions for long-term hydrothermal reactions and heat conduits, contributing to the formation of large VMS deposits [59].

7.2. Chronology and Tectonic Implications of the Hongtoushan Deposit

The Hongtoushan Cu-Zn deposit is a typical VMS deposit and has undergone multiple deformation and metamorphic events since its formation. The ore bodies that form the deposit are generally stratified and controlled by the rhythmic member host rocks in the Hongtoushan formation [22]. This indicates that the formation age of the host rocks should be consistent with the formation age of the VMS deposit. The age determination of the ore-bearing host rocks is of great significance for constraining the formation time of the Hongtoushan VMS deposit. However, multiple episodes of high-grade metamorphism and deformation make isotopic age determination complex. Zircon has a very high Hf content and relatively low Hf diffusion, and the Hf isotope ratios are significantly insensitive to high-grade deformation and alteration [66]. By combining this with the results of the zircon U-Pb dating and Hf isotopes, as well as the geochemistry of the ore-bearing host rocks, we aimed to determine the chronology of the Hongtoushan VMS deposit.

Based on the results, the zircons in the amphibole plagioclase gneiss sample are concentrated around the age of ~2.5 Ga. The zircons have clear microscopic characteristics of magmatic origin, with a narrow and concentrated Th/U content ratio. Thus, the age of 2593 ± 11 – 2510.5 ± 3.9 Ma can approximately represent the formation age of amphibole plagioclase gneiss, and 2526 ± 13 – 2472 ± 20 Ma can approximately represent the metamorphic age of amphibole plagioclase gneiss. In biotite plagioclase gneiss, most zircons have already undergone metamorphism, and some retain inherited cores, showing a consistent metamorphic age of 2471.8 ± 2.6 – 2468.5 ± 2.4 Ma. When comparing the younger ages of the amphibolite plagioclase gneiss (2510.5 ± 3.9 Ma in sample HTS-1605-6) with the core points of the biotite plagioclase gneiss (2509.0 ± 5.8 Ma for HTS-1605-3), it can be reasonably interpreted that the zircon cores in the biotite plagioclase gneiss are more likely inherited from the grains of the amphibolite plagioclase gneiss. Collectively, a compilation of the available zircon geochronology results reveals that the ore-bearing host rocks in the Hongtoushan deposit erupted from 2.59 to 2.51 Ga and then underwent metamorphism from 2.52 to 2.47 Ga. The emplacement and metamorphic events of volcanic rocks were almost continuous, which corresponds with the widespread thermal events at 2.5 Ga in the North China Craton.

In the age histograms (Figure 18B,D), the U-Pb zircon ages of the host rocks display a peak at about 2.52–2.5 Ga, one Hf isotope single-stage model age (TDM1) peak at about 2.6–2.52 Ga, and two Hf isotope two-stage model age (TDM2) peaks at about 2.62–2.52 Ga and 2.7–2.65 Ga, respectively (Figure 18). The first peak of the two-stage model ages (TDM2) almost coincides with the peak of the single-stage model ages (TDM1), which suggests a short residence time of the parent rocks in the crust and the differentiation of the crust and mantle at about 2.520–2.6 Ga. This corresponds to the ~2.62.5 Ga crustal growth event in the North China Craton that was identified in previous studies [67–69]. It is worth noting that we observed another two-stage model age peak at around 2.8–2.7 Ga, which corresponds to another juvenile crust-forming period for the North China Craton [70].

In our research, all of the zircons have relatively high, positive $\epsilon\text{Hf(t)}$ values (3.07–10.45). The two types of host rocks all have higher Hf TDM1 ages than formation ages; this may indicate that the magma source region is contaminated by crustal material or originates from an enriched mantle [71]. In the $\epsilon\text{Hf(t)}$ versus U-Pb age diagram (Figure 18A), most samples fall between the depleted mantle and chondrite evolution lines, while a few fall above the depleted mantle. In the $^{176}\text{Hf}/^{177}\text{Hf}$ versus $^{207}\text{Pb}/^{206}\text{Pb}$ diagram Figure 18B, almost all the zircons show relatively higher initial ($^{176}\text{Hf}/^{177}\text{Hf}$) ratios than the depleted mantle and are distributed between the enriched mantle array and the depleted mantle array. Part of the samples are plotted in the scope of known modern plumes. When combining the discussion of host rock geochemistry, limited crustal contamination is the conclusion. Thus, the relatively high $\epsilon\text{Hf(t)}$ values should come from an enriched mantle source. With the evidence above, this points to a mantle-plume-related event that closely corresponds to volcanism during the ~2.5 Ga mantle plume event, which was global in its extent [72,73].

The formation and preservation of the VMS deposits is influenced by numerous factors such as the source of the metals and sulfur, the tectonic setting, and the ore-forming processes. One of the most important factors is a large stable heat source that can drive a long-lived, high-temperature convective hydrothermal system and has enough permeability to allow for hydrothermal circulation and discharge [62,63].

Based on the geochemistry and chronology results of the ore-bearing host rocks, we are more considerate that the host rocks of the Hongtoushan VMS deposit were generated under a rift environment that was driven by Archean mantle plume activity at 2.6–2.5 Ga. Under the continuous action of the mantle plume, a large amount of mantle-derived magma rose up and caused the partial melting and thinning of the crust, ultimately leading to the formation of rifts and the extensive eruption of volcanic rocks at the seafloor. Due to the good preservation of the VMS deposits, we can say that the rift extensional environment allowed fluid to flow down to the deeper part of the crust and, thus, increase the volume of leaching metals [59]. The subsequent metamorphic deformation brought about structural changes in the primary VMS ore bodies and caused the migration and enrichment of metallic elements, thus forming the ore pillar.

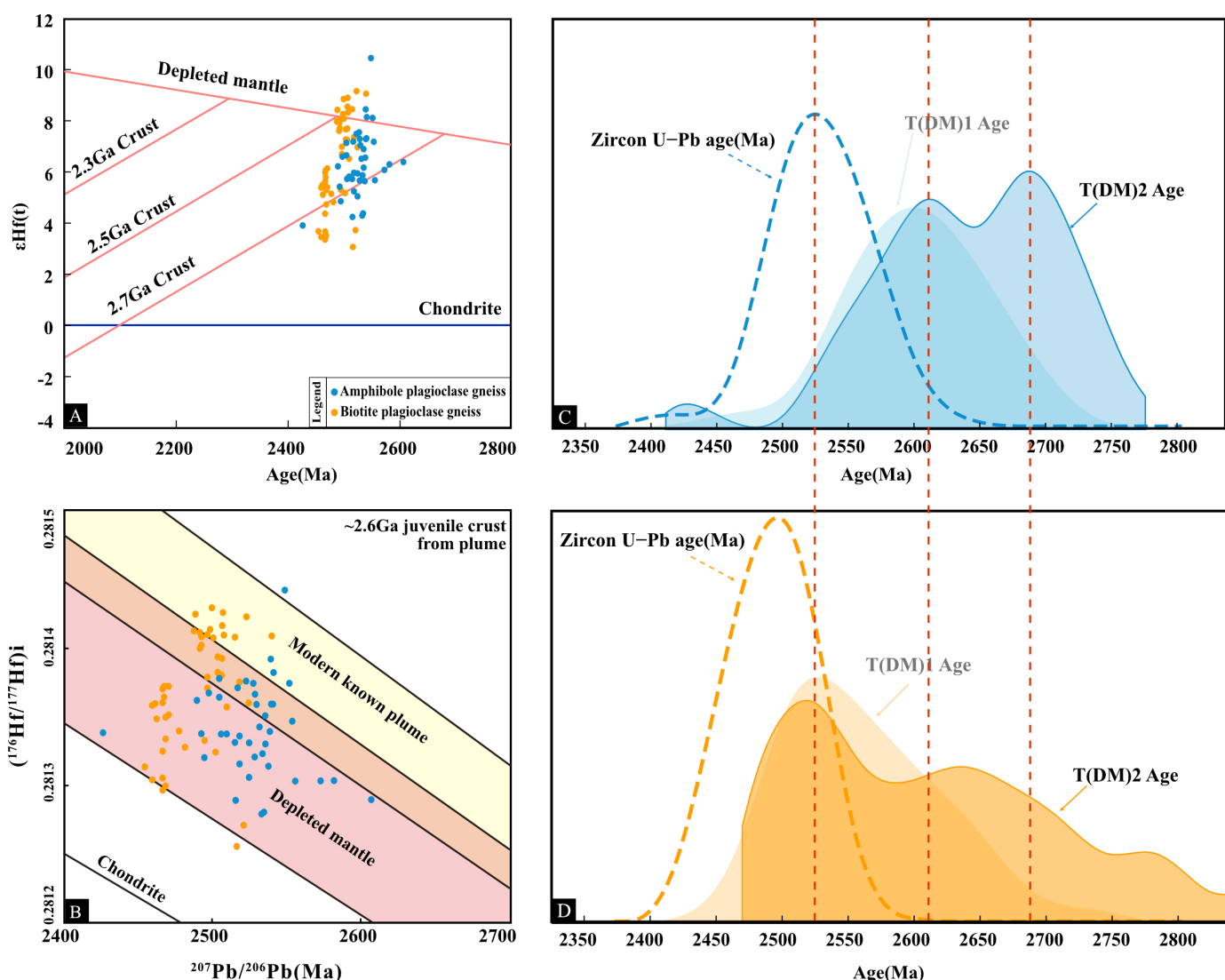


Figure 18. (A) Zircon $\epsilon\text{Hf}(t)$ versus zircon age from the Hongtoushan deposit; the depleted mantle reference lines are from Griffin et al. (2000) [74], and the crustal evolution lines are from Wan et al., 2013 [75]. (B) $^{176}\text{Hf}/^{177}\text{Hf}$ versus $^{207}\text{Pb}/^{206}\text{Pb}$ diagram modified from Zhu et al. (2017) [67]; the line of chondrite is from Blichert-Toft and Albarède (1997) [76], and the fields of depleted mantle and modern known plumes are from Nowell et al. (1998) [77]. (C) Hf isotope TDM1 and TDM2 age histogram of amphibole plagioclase gneiss from the Hongtoushan VMS deposit. (D) Hf isotope one-stage and two-stage modal age histograms of biotite plagioclase gneiss from the Hongtoushan VMS deposit.

8. Conclusions

- (1) The ore-bearing host metamorphic rocks in the Hongtoushan VMS deposit show a continuous variation in composition, with amphibole plagioclase gneiss having a protolith of basalt and the biotite plagioclase gneiss having a protolith of andesite to rhyolite, indicating a volcanic cycle from basic to medium-acidic volcanic rocks.
- (2) The amphibole plagioclase gneiss of the Hongtoushan deposit has a composition resembling contaminated ocean plateau basalt (OPB), which is generally interpreted as being generated from the mantle plume head.
- (3) The petrogenesis of the biotite plagioclase gneiss in the Hongtoushan VMS deposit is interpreted as crustal assimilation combined with the fractional crystallization of basic magma (the magma source of the amphibole plagioclase gneiss) in a rift environment.

- (4) The zircon geochronology indicates that the ore-bearing host rocks in the Hongtoushan deposit were generated between 2.59 and 2.51 Ga, followed by a metamorphic event spanning from 2.52 to 2.47 Ga. The continuous emplacement of volcanic rocks and subsequent metamorphic processes correspond to the 2.5 Ga regional plume-related thermal events of the North China Craton.
- (5) The tectonic setting of the Hongtoushan VMS deposit might be more reasonable due to the rift settings that are related to the ~2.5 Ga global mantle plume activities. The stretching environment provided by rift structures and the high-temperature heat source from the mantle plume activity created ideal conditions for long-term hydrothermal reactions and heat sources, contributing to the formation of the large VMS deposits.

Author Contributions: Conceptualization and writing—original draft preparation, X.Y.; writing—review, editing, and supervision, E.W.; methodology and software, Y.M. and J.F.; validation, K.S. and S.M. All authors have read and agreed to the published version of the manuscript.

Funding: This work was financially supported by the National Natural Science Foundation of China (Grant Number 41372098) and the Fundamental Research Funds for the Central Universities (Grant Number N2123030).

Data Availability Statement: The original contributions presented in the study are included in the article.

Acknowledgments: We thank Beijing GeoAnalysis Co., Ltd., Beijing, China; the Geoanalytical Center of Nuclear Industry in Beijing; the Institute of Geology and Geophysics, Chinese Academy of Sciences (IGGCAS) in Beijing; and Createch Testing Technology Co., Ltd., Beijing for their valuable services and assistance in the data testing conducted for this article. We also thank the Hongtoushan Cu-Zn deposit for their kind help in the field investigations and sampling.

Conflicts of Interest: The authors declare no conflicts of interest.

Abbreviations

The following abbreviations are used in this manuscript:

VMS	Volcanogenic massive sulfide
QGB	Qingyuan granitic-greenstone belt
NCC	North China Craton
REE	Rare earth element
HREE	Heavy rare earth element
LREE	Light rare earth element
LILEs	Large-ion lithophile elements
HFSEs	High-field-strength elements
OIB	Ocean island basalt
OPB	Ocean plateau basalt
ARC	Arc volcanic rock
AFC	Assimilation and fractional crystallization

Appendix A

Table A1. In situ zircon U-Pb isotopic dating data for the ore-bearing metamorphic rocks from the Hongtoushan VMS deposit.

Rock Type	Amphibole Gneiss																
	Point No.	Isotopic Ratio						Isotopic Age (Ma)									
		Size	$^{207}\text{Pb}/^{206}\text{Pb}$	1 σ	$^{207}\text{Pb}/^{235}\text{U}$	1 σ	$^{206}\text{Pb}/^{238}\text{U}$	1 σ	$^{207}\text{Pb}/^{206}\text{Pb}$	1 σ	$^{207}\text{Pb}/^{235}\text{U}$	1 σ	$^{206}\text{Pb}/^{238}\text{U}$	1 σ	Th (ppm)	U (ppm)	Th/U
		μm															
HTS-1605-2-00	100×40	0.1742	0.0044	11.26	0.35	0.4680	0.0120	2581	40	2535	26	2477	48	52.00	84.50	0.615	
HTS-1605-2-01	80×60	0.1697	0.0032	11.47	0.25	0.4924	0.0093	2551	30	2556	20	2578	41	14.10	120.70	0.117	
HTS-1605-2-02	80×35	0.1675	0.0041	10.45	0.26	0.4610	0.0091	2522	42	2475	22	2442	41	35.10	123.80	0.284	
HTS-1605-2-03	120×50	0.1725	0.0035	10.93	0.23	0.4654	0.0076	2572	34	2516	19	2461	34	65.70	135.40	0.485	
HTS-1605-2-04	80×30	0.1752	0.003	11.38	0.20	0.4803	0.0077	2606	27	2552	16	2527	34	215.00	197.00	1.091	
HTS-1605-2-05	80×40	0.1672	0.0023	10.41	0.13	0.4586	0.0059	2529	24	2470	12	2432	26	267.00	373.00	0.716	
HTS-1605-2-06	60×40	0.1702	0.003	10.69	0.22	0.4632	0.0079	2553	29	2495	19	2451	35	123.70	192.00	0.644	
HTS-1605-2-07	80×50	0.1707	0.0054	10.85	0.31	0.4740	0.0150	2555	51	2507	27	2496	65	17.00	158.00	0.108	
HTS-1605-2-08	80×35	0.1625	0.0038	10.41	0.21	0.4760	0.0087	2489	35	2469	18	2508	38	14.30	197.00	0.073	
HTS-1605-2-09	100×40	0.1683	0.0019	10.87	0.15	0.4763	0.0073	2537	19	2512	12	2510	32	144.60	260.00	0.556	
HTS-1605-2-10	90×40	0.1655	0.0036	10.29	0.20	0.4617	0.0073	2504	37	2458	18	2446	33	3.66	192.50	0.019	
HTS-1605-2-11	75×40	0.1674	0.0023	11.23	0.20	0.4800	0.0065	2528	23	2543	15	2525	29	128.00	271.00	0.472	
HTS-1605-2-12	50×30	0.1662	0.0025	10.40	0.15	0.4621	0.0070	2515	25	2469	13	2447	31	60.10	260.00	0.231	
HTS-1605-2-13	60×45	0.1644	0.0023	10.93	0.22	0.4795	0.0088	2504	25	2513	19	2521	38	26.80	181.00	0.148	
HTS-1605-2-14	75×50	0.1686	0.0035	10.51	0.30	0.4590	0.0100	2531	36	2471	21	2431	43	16.00	160.00	0.100	
HTS-1605-2-15	90×40	0.1607	0.0052	9.99	0.35	0.4521	0.0097	2426	64	2436	32	2400	44	23.50	97.00	0.242	
HTS-1605-2-16	60×30	0.1685	0.0034	11.01	0.26	0.4732	0.0081	2534	35	2520	21	2500	37	18.70	98.10	0.191	
HTS-1605-2-17	100×45	0.1685	0.0032	10.53	0.24	0.4605	0.0094	2535	32	2478	21	2439	42	2.20	129.00	0.017	
HTS-1605-2-18	100×35	0.1696	0.0034	10.68	0.23	0.4571	0.0084	2540	33	2492	20	2423	37	40.40	80.30	0.503	
HTS-1605-2-19	60×30	0.1695	0.0031	10.55	0.23	0.4582	0.0084	2548	30	2479	20	2434	35	35.00	125.30	0.279	
HTS-1605-6-02	85×35	0.16514	0.0018	11.63	0.23	0.5105	0.0095	2509	19	2575	19	2659	41	113.95	387.51	0.294	
HTS-1605-6-06	100×35	0.16691	0.0017	11.16	0.18	0.4846	0.0075	2528	17	2537	15	2547	33	106.84	363.72	0.294	
HTS-1605-6-07	80×40	0.16747	0.0019	11.24	0.21	0.4867	0.0090	2532	19	2543	17	2556	39	88.35	769.97	0.115	
HTS-1605-6-09	80×50	0.16807	0.0016	11.28	0.18	0.4864	0.0074	2539	15	2547	15	2555	32	129.02	1118.18	0.115	
HTS-1605-6-11	60×40	0.16823	0.0017	10.76	0.17	0.4630	0.0065	2540	17	2503	15	2453	29	88.74	435.52	0.204	
HTS-1605-6-13	90×40	0.16772	0.0015	10.48	0.19	0.4523	0.0073	2535	15	2478	16	2405	32	134.00	714.81	0.187	
HTS-1605-6-14	90×35	0.16803	0.0015	10.71	0.19	0.4621	0.0078	2538	15	2499	16	2449	34	219.04	403.68	0.543	
HTS-1605-6-15	45×35	0.16692	0.0016	11.07	0.19	0.4801	0.0067	2527	10	2529	16	2528	29	76.78	553.58	0.139	
HTS-1605-6-16	80×30	0.16755	0.0016	10.52	0.16	0.4549	0.0058	2533	16	2482	14	2417	26	158.16	496.83	0.318	
HTS-1605-6-17	90×50	0.16480	0.0018	10.38	0.17	0.4565	0.0062	2505	18	2469	15	2424	27	136.93	556.67	0.246	
HTS-1605-6-18	80×45	0.16597	0.0016	10.30	0.20	0.4498	0.0075	2518	49	2462	18	2394	33	100.78	428.99	0.235	
HTS-1605-6-19	60×40	0.16473	0.0019	10.32	0.22	0.4543	0.0085	2505	18	2464	20	2414	38	84.38	261.33	0.323	
HTS-1605-6-20	80×40	0.16649	0.0018	10.42	0.17	0.4538	0.0065	2524	17	2472	15	2412	29	153.94	524.92	0.293	
HTS-1605-9-19	130×40	0.1641	0.0025	10.55	0.18	0.4603	0.0079	2499	25	2479	16	2442	33	10.20	233.00	0.044	
HTS-1605-9-29	100×45	0.1662	0.0024	11.25	0.22	0.4898	0.0075	2512	25	2541	18	2567	32	6.35	125.40	0.051	
HTS-1605-9-27	100×25	0.1643	0.0023	10.48	0.14	0.4591	0.0063	2497	23	2476	13	2433	28	10.19	154.60	0.066	
HTS-1605-9-5	110×50	0.1663	0.0023	12.02	0.42	0.5130	0.0140	2529	23	2604	28	2664	57	26.00	430.00	0.060	
HTS-1605-9-18	100×45	0.1695	0.0025	10.36	0.21	0.4389	0.0087	2554	23	2464	19	2341	39	30.30	151.10	0.201	
HTS-1605-9-11	100×35	0.1707	0.0045	11.93	0.36	0.4930	0.0110	2560	50	2588	25	2579	45	12.70	103.00	0.123	
HTS-1605-9-24	105×40	0.1654	0.0041	10.56	0.36	0.4640	0.0110	2494	45	2485	29	2452	47	11.30	88.10	0.128	
HTS-1605-9-26	130×20	0.1717	0.0028	10.86	0.20	0.4566	0.0079	2565	27	2507	17	2421	35	18.07	110.30	0.164	
HTS-1605-9-13	100×25	0.1692	0.0028	10.87	0.19	0.4607	0.0061	2544	27	2509	17	2441	27	20.78	96.40	0.216	
HTS-1605-9-4	110×35	0.1673	0.0019	11.40	0.17	0.4882	0.0059	2528	20	2553	14	2561	25	52.50	162.00	0.324	

Table A1. Cont.

Rock Type	Amphibole Gneiss															
	Point No.	Size		Isotopic Ratio						Isotopic Age (Ma)						
		μm	207Pb/206Pb	1σ	207Pb/235U	1σ	206Pb/238U	1σ	207Pb/206Pb	1σ	207Pb/235U	1σ	206Pb/238U	1σ	Th (ppm)	U (ppm)
HTS-1605-9-16	120×30	0.1704	0.0045	12.35	0.36	0.5070	0.0120	2537	50	2620	29	2665	54	15.32	42.40	0.361
HTS-1605-9-15	100×35	0.1702	0.0042	10.91	0.25	0.4627	0.0091	2560	43	2519	21	2453	39	27.60	77.20	0.358
HTS-1605-9-2	150×45	0.1669	0.0011	10.90	0.13	0.4678	0.0050	2524	11	2513	10	2473	22	272.00	646.00	0.421
HTS-1605-9-25	100×35	0.1883	0.0063	13.35	0.47	0.5140	0.0120	2683	56	2687	33	2666	53	16.16	36.10	0.448
HTS-1605-9-20	120×50	0.1746	0.0043	11.20	0.30	0.4650	0.0120	2588	39	2530	25	2452	54	19.30	44.80	0.431
HTS-1605-9-28	100×25	0.1725	0.0020	11.25	0.14	0.4699	0.0055	2577	19	2542	11	2481	24	124.40	212.00	0.587
HTS-1605-9-10	100×50	0.167	0.0035	10.96	0.29	0.4750	0.0120	2515	34	2519	23	2510	46	39.30	66.90	0.587
HTS-1605-9-12	100×35	0.172	0.0050	10.83	0.23	0.4529	0.0080	2561	40	2513	19	2410	34	152.00	168.00	0.905
HTS-1605-9-17	100×40	0.1635	0.0013	9.52	0.09	0.4126	0.0040	2492	12	2388.1	8.4	2226	18	978.00	1039.00	0.941
HTS-1605-1-01	70×35	0.1616	0.0015	10.13	0.10	0.4529	0.0037	2470	16	2445	9.6	2407	17	115.00	532.00	0.216
HTS-1605-1-02	70×35	0.1610	0.0017	10.63	0.12	0.4777	0.0042	2462	18	2490	10	2516	18	7.60	421.00	0.018
HTS-1605-1-03	80×30	0.1628	0.0022	10.03	0.13	0.4502	0.0046	2481	23	2436	12	2396	20	152.00	486.00	0.313
HTS-1605-1-04	60×40	0.1615	0.0017	10.40	0.14	0.4705	0.0049	2468	18	2469	12	2485	21	15.00	479.00	0.031
HTS-1605-1-05	90×40	0.1610	0.0010	10.69	0.08	0.4783	0.0034	2466	11	2495.7	6.8	2519	15	17.80	1001.00	0.018
HTS-1605-1-06	60×35	0.1617	0.0013	10.51	0.08	0.4695	0.0034	2470	13	2480.1	7.4	2481	15	10.34	697.00	0.015
HTS-1605-1-07	80×50	0.1606	0.0012	10.32	0.11	0.4638	0.0046	2459	12	2462	10	2455	20	17.40	988.00	0.018
HTS-1605-1-08	70×40	0.1612	0.0012	11.04	0.10	0.4951	0.0034	2466	12	2525.5	8.5	2592	15	20.20	689.00	0.029
HTS-1605-1-09	60×30	0.1614	0.0026	10.13	0.17	0.4583	0.0051	2467	28	2445	16	2432	23	22.90	576.00	0.040
HTS-1605-1-10	60×30	0.1605	0.0014	10.63	0.09	0.4810	0.0038	2459	15	2490.6	8.1	2531	17	23.00	851.00	0.027
HTS-1605-1-11	90×45	0.1611	0.0011	9.94	0.10	0.4470	0.0042	2466	12	2428.3	9.5	2381	19	19.40	949.00	0.020
HTS-1605-1-12	60×40	0.1613	0.0019	9.96	0.13	0.4491	0.0054	2466	21	2428	12	2390	24	175.00	400.00	0.438
HTS-1605-1-13	60×35	0.1613	0.0010	10.15	0.10	0.4533	0.0032	2468	10	2447.5	8.7	2410	14	18.04	1269.00	0.014
HTS-1605-1-14	60×35	0.1602	0.0014	10.01	0.10	0.4505	0.0043	2454	16	2434	8.8	2399	19	20.50	643.00	0.032
HTS-1605-1-15	90×50	0.1615	0.0014	10.35	0.09	0.4636	0.0035	2468	14	2467.7	8.9	2455	15	19.55	678.00	0.029
HTS-1605-1-16	80×35	0.1611	0.0015	9.94	0.11	0.4520	0.0055	2466	15	2429	10	2404	24	25.70	2060.00	0.012
HTS-1605-1-17	60×30	0.1623	0.0018	10.38	0.12	0.4631	0.0058	2477	19	2467	11	2451	25	7.61	385.00	0.020
HTS-1605-1-18	60×40	0.1608	0.0014	10.43	0.10	0.4693	0.0042	2461	14	2472	8.7	2480	18	24.30	851.00	0.029
HTS-1605-1-19	75×40	0.1612	0.0012	10.29	0.12	0.4587	0.0044	2467	13	2459	10	2433	19	26.00	775.00	0.034
HTS-1605-3-01	40×30	0.1650	0.0019	10.75	0.23	0.4723	0.0091	2507	20	2502	19	2494	40	8.60	493.84	0.017
HTS-1605-3-02	80×25	0.1658	0.0018	10.58	0.21	0.4628	0.0089	2516	51	2487	19	2452	39	14.75	611.73	0.024
HTS-1605-3-03	110×40	0.1657	0.0016	11.06	0.24	0.4840	0.0101	2515	17	2528	20	2545	44	33.02	725.03	0.046
HTS-1605-3-04	50×40	0.1660	0.0015	10.83	0.16	0.4727	0.0061	2518	15	2508	13	2495	27	7.00	551.71	0.013
HTS-1605-3-07	60×25	0.1644	0.0019	10.43	0.21	0.4599	0.0092	2502	19	2473	19	2439	41	8.73	403.07	0.022
HTS-1605-3-10	70×30	0.1666	0.0020	11.39	0.19	0.4959	0.0075	2524	20	2556	15	2596	32	5.57	447.62	0.012
HTS-1605-3-11	60×40	0.1639	0.0017	10.92	0.18	0.4832	0.0073	2496	17	2517	15	2541	32	25.52	862.38	0.030
HTS-1605-3-12	40×35	0.1661	0.0015	11.22	0.21	0.4895	0.0086	2520	48	2542	18	2568	37	5.04	483.95	0.010
HTS-1605-3-13	90×40	0.1639	0.0020	10.71	0.25	0.4738	0.0104	2496	21	2499	22	2500	45	4.61	391.94	0.012
HTS-1605-3-14	90×40	0.1633	0.0016	10.45	0.16	0.4640	0.0062	2500	17	2476	14	2457	27	26.38	715.33	0.037
HTS-1605-3-15	70×50	0.1640	0.0016	10.82	0.17	0.4778	0.0067	2498	15	2507	15	2518	29	48.23	845.55	0.057
HTS-1605-3-16	40×30	0.1648	0.0017	10.50	0.14	0.4620	0.0057	2506	18	2480	12	2448	25	2.28	485.96	0.005
HTS-1605-3-17	60×35	0.1642	0.0015	10.44	0.15	0.4608	0.0057	2499	17	2475	13	2443	25	11.96	606.90	0.020
HTS-1605-3-18	40×25	0.1649	0.0018	10.37	0.23	0.4561	0.0097	2506	19	2469	20	2422	43	12.22	1200.06	0.010
HTS-1605-3-19	90×40	0.1651	0.0017	10.75	0.17	0.4719	0.0063	2509	17	2502	14	2492	28	15.85	522.46	0.030
HTS-1605-8-00	40×30	0.1620	0.0010	10.14	0.10	0.4520	0.0054	2474	11	2446	9.2	2402	24	68.20	543.00	0.126
HTS-1605-8-01	40×25	0.1616	0.0015	10.09	0.10	0.4525	0.0039	2469	16	2442	8.9	2405	17	27.90	56.00	0.498

Table A1. Cont.

Rock Type	Biotite-Rich Gneiss															
	Point No.	Isotopic Ratio						Isotopic Age (Ma)								
		Size	$^{207}\text{Pb}/^{206}\text{Pb}$	1σ	$^{207}\text{Pb}/^{235}\text{U}$	1σ	$^{206}\text{Pb}/^{238}\text{U}$	1σ	$^{207}\text{Pb}/^{206}\text{Pb}$	1σ	$^{207}\text{Pb}/^{235}\text{U}$	1σ	$^{206}\text{Pb}/^{238}\text{U}$	1σ	Th (ppm)	U (ppm)
HTS-1605-8-03	75×40	0.1663	0.0016	10.15	0.12	0.4464	0.0055	2518	16	2449	10	2378	24	39.00	82.10	0.475
HTS-1605-8-04	80×35	0.1654	0.0016	10.11	0.11	0.4413	0.0057	2507	16	2443	9.6	2358	25	73.60	122.60	0.600
HTS-1605-8-05	60×50	0.1618	0.0015	10.56	0.13	0.4643	0.0047	2470	16	2483	11	2457	20	58.60	116.90	0.501
HTS-1605-8-06	70×45	0.1651	0.0013	10.19	0.10	0.4479	0.0049	2506	13	2451	8.9	2388	21	54.10	108.50	0.499
HTS-1605-8-07	40×30	0.1635	0.0014	10.04	0.09	0.4455	0.0049	2492	15	2437	8.5	2374	22	50.00	461.00	0.108
HTS-1605-8-08	60×45	0.1642	0.0032	10.24	0.22	0.4546	0.0073	2491	33	2451	20	2413	33	74.70	535.00	0.140
HTS-1605-8-09	70×50	0.1670	0.0036	10.26	0.25	0.4487	0.0095	2518	35	2454	23	2385	42	36.30	86.30	0.421
HTS-1605-8-10	40×25	0.1647	0.0028	10.78	0.24	0.4697	0.0085	2503	27	2505	20	2484	35	35.10	84.80	0.414
HTS-1605-8-11	40×30	0.1634	0.0033	10.29	0.21	0.4574	0.0084	2475	35	2457	19	2424	37	52.50	98.20	0.535
HTS-1605-8-13	40×25	0.1648	0.0035	10.20	0.22	0.4525	0.0095	2492	35	2447	20	2402	42	21.20	48.10	0.441
HTS-1605-8-14	60×40	0.1642	0.0030	9.99	0.17	0.4470	0.0073	2491	30	2433	17	2380	33	35.60	71.60	0.497
HTS-1605-8-15	70×40	0.1639	0.0035	10.09	0.22	0.4502	0.0072	2488	35	2437	20	2394	32	43.70	100.90	0.433
HTS-1605-8-16	40×25	0.1657	0.0035	10.60	0.22	0.4639	0.0076	2503	35	2483	19	2454	34	63.80	487.00	0.131
HTS-1605-8-17	80×50	0.1699	0.0047	10.88	0.32	0.4700	0.0110	2550	43	2507	26	2476	49	54.90	125.20	0.438
HTS-1605-8-18	40×30	0.1605	0.0036	10.50	0.29	0.4627	0.0090	2449	40	2478	24	2449	40	107.70	220.80	0.488
HTS-1605-8-19	70×40	0.1628	0.0029	10.03	0.16	0.4565	0.0065	2477	30	2435	15	2423	29	48.80	96.70	0.505
HTS-1605-8-2	60×50	0.1640	0.0030	10.16	0.21	0.4512	0.0079	2487	31	2447	19	2398	35	28.57	72.70	0.393
HTS-1605-8-20	60×45	0.1675	0.0038	10.06	0.25	0.4455	0.0087	2521	38	2438	24	2373	39	333.20	285.10	1.169
HTS-1605-8-21	70×40	0.1627	0.0040	10.36	0.32	0.4560	0.0100	2479	42	2461	29	2416	44	50.30	99.90	0.504
HTS-1605-8-22	60×45	0.1650	0.0030	10.38	0.18	0.4562	0.0065	2496	30	2467	16	2425	29	28.90	59.50	0.486
HTS-1605-8-23	60×40	0.1646	0.0037	10.35	0.25	0.4571	0.0079	2488	37	2459	22	2429	36	40.40	88.90	0.454
HTS-1605-8-25	60×50	0.1635	0.0035	10.20	0.24	0.4544	0.0087	2478	36	2450	21	2411	39	96.10	844.00	0.114
HTS-1605-8-26	40×30	0.1657	0.0032	10.13	0.22	0.4458	0.0081	2509	33	2444	21	2374	36	46.10	77.90	0.592
HTS-1605-8-27	70×30	0.1625	0.0041	9.80	0.26	0.4408	0.0094	2475	45	2408	24	2350	42	60.60	454.00	0.133
HTS-1605-8-28	40×30	0.1665	0.0022	10.49	0.16	0.4554	0.0058	2516	22	2476	14	2417	26	232.00	228.00	1.018
HTS-1605-8-29	50×40	0.1662	0.0020	10.05	0.14	0.4406	0.0059	2514	21	2439	13	2352	26	31.40	91.20	0.344

Table A2. In situ zircon Lu-Hf isotopic dating data for ore-bearing metamorphic rocks from the Hongtoushan VMS deposit.

Rock Type	Amphibole Plagioclase Gneiss											
	Point No.	$^{176}\text{Hf}/^{177}\text{Hf}(\text{corr})$	2σ	$^{176}\text{Yb}/^{177}\text{Hf}(\text{corr})$	2σ	$^{176}\text{Lu}/^{177}\text{Hf}(\text{corr})$	2σ	Age (Ma)	Hf(I)	$\epsilon\text{Hf(t)}$	2σ	T(DM)1
HTS-1605-2-00	0.281462	0.000022	0.090815	0.002101	0.003216	0.000060	2581	0.281303277	6.30	0.77	2654.97	2692.22
HTS-1605-2-01	0.281532	0.000019	0.103208	0.000438	0.003239	0.000013	2551	0.281374071	8.11	0.69	2555.06	2557.10
HTS-1605-2-02	0.281512	0.000015	0.087215	0.002007	0.002838	0.000056	2522	0.281375644	7.49	0.55	2555.07	2572.25
HTS-1605-2-03	0.281391	0.000015	0.052962	0.000678	0.001796	0.000018	2572	0.281303095	6.08	0.55	2652.80	2698.39
HTS-1605-2-04	0.281454	0.000020	0.091507	0.002488	0.003292	0.000090	2606	0.281289434	6.39	0.72	2672.88	2706.35
HTS-1605-2-05	0.281442	0.000012	0.045685	0.000794	0.001720	0.000022	2529	0.281358666	7.05	0.44	2577.36	2604.81
HTS-1605-2-06	0.281469	0.000018	0.076365	0.004351	0.002507	0.000087	2553	0.281346475	7.18	0.63	2594.08	2616.02
HTS-1605-2-07	0.281480	0.000017	0.106880	0.000699	0.003620	0.000025	2555	0.281302928	5.68	0.59	2659.04	2709.64
HTS-1605-2-08	0.281445	0.000016	0.051804	0.001589	0.001743	0.000051	2489	0.281361615	6.22	0.55	2575.19	2624.02
HTS-1605-2-09	0.281381	0.000013	0.039216	0.000519	0.001389	0.000019	2537	0.281313766	5.64	0.45	2638.52	2697.57
HTS-1605-2-10	0.281622	0.000024	0.148214	0.004311	0.005110	0.000107	2504	0.281377552	7.14	0.86	2557.16	2579.62

Table A2. Cont.

HTS-1605-2-11	0.281490	0.000013	0.082011	0.001065	0.002564	0.000025	2528	0.281366099	7.29	0.48	2567.98	2589.23
HTS-1605-2-12	0.281403	0.000016	0.072652	0.002301	0.002373	0.000047	2515	0.281288943	4.24	0.56	2677.85	2765.73
HTS-1605-2-13	0.281523	0.000019	0.102740	0.002231	0.003320	0.000074	2504	0.281363898	6.65	0.68	2574.32	2609.42
HTS-1605-2-14	0.281492	0.000019	0.103751	0.008730	0.003093	0.000208	2531	0.281342311	6.51	0.69	2602.71	2639.20
HTS-1605-2-15	0.281490	0.000021	0.107443	0.000998	0.003277	0.000030	2426	0.281338076	3.91	0.75	2619.01	2715.70
HTS-1605-2-16	0.281398	0.000018	0.074308	0.000721	0.002430	0.000018	2534	0.281280348	4.38	0.64	2689.00	2772.27
HTS-1605-2-17	0.281524	0.000020	0.121214	0.001880	0.003994	0.000049	2535	0.281329946	6.17	0.69	2622.45	2663.59
HTS-1605-2-18	0.281503	0.000017	0.097070	0.001207	0.002961	0.000030	2540	0.281358889	7.31	0.62	2577.82	2597.27
HTS-1605-2-19	0.281660	0.000020	0.139638	0.000948	0.004481	0.000034	2548	0.281441776	10.45	0.71	2453.57	2411.13
HTS-1605-6-01	0.281436	0.000020	0.080829	0.000249	0.002500	0.000010	2518	0.281315402	5.24	0.70	2640.69	2706.44
HTS-1605-6-02	0.281469	0.000015	0.081937	0.000756	0.002757	0.000034	2509	0.28133723	5.82	0.54	2611.01	2664.40
HTS-1605-6-03	0.281497	0.000015	0.075977	0.000481	0.002633	0.000021	2516	0.281370827	7.19	0.53	2562.17	2586.38
HTS-1605-6-06	0.281411	0.000015	0.060628	0.001778	0.001882	0.000050	2528	0.281320488	5.66	0.55	2630.98	2688.84
HTS-1605-6-07	0.281360	0.000019	0.045030	0.000538	0.001669	0.000033	2532	0.281279038	4.30	0.67	2687.69	2776.15
HTS-1605-6-08	0.281421	0.000014	0.057082	0.000610	0.001865	0.000015	2515	0.281331049	5.73	0.48	2616.87	2674.33
HTS-1605-6-09	0.281547	0.000017	0.102952	0.001662	0.003201	0.000055	2539	0.281391646	8.45	0.60	2530.68	2526.70
HTS-1605-6-11	0.281548	0.000015	0.110331	0.001583	0.003415	0.000044	2540	0.281381895	8.14	0.54	2544.69	2546.80
HTS-1605-6-12	0.281472	0.000015	0.069006	0.001183	0.002329	0.000037	2539	0.281358889	7.29	0.54	2577.23	2597.99
HTS-1605-6-13	0.281463	0.000016	0.071177	0.000801	0.002326	0.000012	2535	0.281350427	6.89	0.56	2589.45	2619.02
HTS-1605-6-14	0.281430	0.000016	0.056875	0.001256	0.001876	0.000030	2538	0.281338899	6.56	0.58	2604.60	2641.98
HTS-1605-6-15	0.281518	0.000017	0.091119	0.000537	0.002972	0.000019	2527	0.281374046	7.55	0.59	2557.09	2572.63
HTS-1605-6-16	0.281428	0.000019	0.067072	0.001289	0.002170	0.000036	2533	0.281322855	5.87	0.66	2628.16	2680.32
HTS-1605-6-17	0.281448	0.000017	0.075471	0.001236	0.002319	0.000031	2505	0.281337128	5.73	0.59	2610.15	2667.00
HTS-1605-6-18	0.281413	0.000013	0.044729	0.000359	0.001614	0.000010	2518	0.281335715	5.97	0.46	2609.56	2662.18
HTS-1605-6-20	0.281383	0.000014	0.033060	0.001012	0.001080	0.000028	2524	0.281330788	5.94	0.51	2614.80	2668.76
HTS-1605-9-02	0.281412	0.000018	0.069771	0.000936	0.002197	0.000027	2524	0.281305635	5.05	0.62	2653.02	2723.62
HTS-1605-9-17	0.281434	0.000014	0.060028	0.000242	0.002024	0.000012	2492	0.281337371	5.43	0.49	2609.70	2674.96
HTS-1605-9-24	0.281423	0.000019	0.057881	0.000408	0.002151	0.000024	2494	0.281319994	4.85	0.66	2634.44	2711.56
HTS-1605-9-27	0.281473	0.000015	0.070560	0.003366	0.002222	0.000102	2497	0.281367013	6.60	0.53	2568.22	2607.11

Rock Type	Biotite Plagioclase Gneiss											
Point No.	$^{176}\text{Hf}/^{177}\text{Hf}(\text{corr})$	2σ	$^{176}\text{Yb}/^{177}\text{Hf}(\text{corr})$	2σ	$^{176}\text{Lu}/^{177}\text{Hf}(\text{corr})$	2σ	Age (Ma)	Hf(I)	$\epsilon\text{Hf(t)}$	2σ	T(DM)1	T(DM)2
HTS-1605-1-00	0.281355	0.000017	0.002748	0.000053	0.000092	0.000003	2470	0.28135	5.40	0.61	2585.49	2659.07
HTS-1605-1-02	0.281352	0.000014	0.002509	0.000073	0.000074	0.000003	2462	0.28135	5.11	0.51	2589.37	2670.62
HTS-1605-1-03	0.281344	0.000014	0.010610	0.000065	0.000337	0.000003	2481	0.28133	4.82	0.49	2617.73	2703.41
HTS-1605-1-04	0.281342	0.000021	0.005798	0.000102	0.000182	0.000004	2468	0.28133	4.73	0.74	2609.28	2698.74
HTS-1605-1-05	0.281301	0.000019	0.002694	0.000078	0.000089	0.000003	2466	0.28130	3.36	0.68	2658.42	2781.03
HTS-1605-1-06	0.281376	0.000014	0.002592	0.000053	0.000084	0.000002	2470	0.28137	6.14	0.48	2557.85	2613.85
HTS-1605-1-07	0.281309	0.000013	0.003350	0.000287	0.000111	0.000011	2459	0.28130	3.46	0.46	2648.64	2769.29
HTS-1605-1-08	0.281407	0.000020	0.028319	0.000834	0.000994	0.000030	2466	0.28136	5.62	0.71	2576.31	2642.33
HTS-1605-1-09	0.281386	0.000017	0.009367	0.000608	0.000294	0.000019	2467	0.28137	6.07	0.61	2558.37	2615.79
HTS-1605-1-10	0.281362	0.000013	0.002733	0.000091	0.000079	0.000003	2459	0.28136	5.39	0.46	2576.30	2651.10
HTS-1605-1-11	0.281390	0.000015	0.012472	0.000055	0.000433	0.000002	2466	0.28137	5.98	0.54	2561.27	2620.58
HTS-1605-1-12	0.281309	0.000018	0.002473	0.000065	0.000076	0.000002	2466	0.28131	3.67	0.64	2646.61	2761.80
HTS-1605-1-13	0.281303	0.000017	0.002744	0.000076	0.000079	0.000003	2468	0.28130	3.51	0.60	2654.29	2773.08
HTS-1605-1-14	0.281318	0.000012	0.003797	0.000105	0.000101	0.000003	2454	0.28131	3.68	0.42	2635.92	2751.74
HTS-1605-1-15	0.281354	0.000014	0.003552	0.000087	0.000104	0.000003	2468	0.28135	5.29	0.49	2587.89	2664.21
HTS-1605-1-16	0.281327	0.000011	0.002083	0.000039	0.000056	0.000002	2466	0.28132	4.37	0.38	2620.55	2719.25
HTS-1605-1-17	0.281346	0.000020	0.004076	0.000082	0.000151	0.000003	2477	0.28134	5.14	0.70	2601.40	2680.35

Table A2. *Cont.*

HTS-1605-1-18	0.281395	0.000012	0.023257	0.001504	0.000751	0.000053	2461	0.28136	5.48	0.42	2576.61	2647.01
HTS-1605-1-19	0.281385	0.000016	0.013823	0.000218	0.000454	0.000006	2467	0.28136	5.79	0.58	2569.24	2632.80
HTS-1605-3-01	0.281425	0.000017	0.007169	0.000021	0.000326	0.000002	2507	0.28141	8.33	0.62	2508.14	2508.79
HTS-1605-3-02	0.281393	0.000024	0.078793	0.000869	0.002859	0.000026	2516	0.28126	3.07	0.84	2728.02	2838.15
HTS-1605-3-03	0.281440	0.000020	0.015378	0.000059	0.000680	0.000003	2515	0.28141	8.45	0.70	2510.04	2507.31
HTS-1605-3-04	0.281423	0.000019	0.021087	0.000073	0.001000	0.000005	2518	0.28137	7.36	0.68	2554.45	2576.51
HTS-1605-3-05	0.281404	0.000020	0.037821	0.002367	0.001510	0.000094	2494	0.28133	5.30	0.72	2614.78	2684.33
HTS-1605-3-06	0.281405	0.000022	0.011852	0.000244	0.000527	0.000012	2506	0.28138	7.25	0.77	2547.64	2573.66
HTS-1605-3-07	0.281345	0.000016	0.009982	0.000187	0.000438	0.000008	2502	0.28132	5.17	0.56	2622.61	2697.95
HTS-1605-3-08	0.281446	0.000021	0.012533	0.000098	0.000499	0.000005	2522	0.28142	9.16	0.74	2489.97	2469.98
HTS-1605-3-09	0.281437	0.000025	0.015086	0.000053	0.000582	0.000004	2539	0.28141	9.06	0.90	2508.47	2489.54
HTS-1605-3-10	0.281382	0.000016	0.011479	0.000114	0.000468	0.000003	2524	0.28136	6.97	0.55	2574.37	2605.79
HTS-1605-3-11	0.281402	0.000019	0.013770	0.000069	0.000658	0.000004	2496	0.28137	6.70	0.69	2560.47	2599.99
HTS-1605-3-12	0.281434	0.000019	0.080779	0.000900	0.003389	0.000032	2520	0.28127	3.72	0.66	2708.36	2801.63
HTS-1605-3-13	0.281436	0.000017	0.015201	0.000300	0.000554	0.000008	2496	0.28141	8.08	0.60	2507.85	2515.17
HTS-1605-3-14	0.281433	0.000018	0.013912	0.000196	0.000548	0.000005	2500	0.28141	8.09	0.64	2510.98	2517.76
HTS-1605-3-15	0.281436	0.000017	0.011147	0.000223	0.000476	0.000004	2498	0.28141	8.26	0.61	2502.67	2505.66
HTS-1605-3-16	0.281408	0.000018	0.007558	0.000049	0.000333	0.000003	2506	0.28139	7.70	0.63	2530.89	2546.58
HTS-1605-3-17	0.281449	0.000019	0.010315	0.000255	0.000424	0.000007	2499	0.28143	8.85	0.67	2481.51	2470.57
HTS-1605-3-18	0.281451	0.000020	0.012448	0.000153	0.000541	0.000008	2506	0.28143	8.90	0.70	2486.01	2473.36
HTS-1605-8-03	0.281423	0.000019	0.018248	0.000272	0.000863	0.000015	2503	0.28138	7.27	0.68	2545.10	2570.54
HTS-1605-8-04	0.281382	0.000016	0.013437	0.000123	0.000532	0.000004	2509	0.28136	6.51	0.55	2578.64	2621.70
HTS-1605-8-05	0.281402	0.000019	0.011238	0.000052	0.000490	0.000003	2496	0.28138	6.99	0.69	2549.40	2582.51
HTS-1605-8-06	0.281434	0.000019	0.010505	0.000171	0.000463	0.000010	2487	0.28141	7.97	0.66	2504.23	2514.93
HTS-1605-8-08	0.281436	0.000017	0.010152	0.000048	0.000414	0.000001	2506	0.28142	8.55	0.60	2498.84	2494.38
HTS-1605-8-09	0.281433	0.000018	0.016439	0.000090	0.000661	0.000004	2492	0.28140	7.72	0.64	2518.35	2534.49
HTS-1605-8-12	0.281436	0.000017	0.017608	0.001414	0.000589	0.000037	2492	0.28141	7.93	0.61	2509.98	2521.05
HTS-1605-8-15	0.281408	0.000018	0.007144	0.000106	0.000311	0.000008	2503	0.28139	7.67	0.63	2529.48	2546.10
HTS-1605-8-17	0.281449	0.000019	0.021832	0.001628	0.000803	0.000047	2491	0.28141	8.02	0.67	2505.93	2514.98
HTS-1605-8-23	0.281451	0.000020	0.013019	0.000296	0.000570	0.000010	2488	0.28142	8.42	0.70	2487.89	2487.82
HTS-1605-8-29	0.281423	0.000019	0.011692	0.000057	0.000502	0.000002	2491	0.28140	7.61	0.68	2521.41	2540.26

Table A3. Major (wt%) element compositions and trace (rare earth) element (ppm) compositions of the ore-bearing metamorphic rocks from the Hongtoushan VMS deposit.

Rock Type		Amphibole Plagioclase Gneiss														
No.		Al ₂ O ₃	BaO	CaO	Cr ₂ O ₃	Fe ₂ O ₃ T	K ₂ O	MgO	MnO	Na ₂ O	P ₂ O ₅	SiO ₂	SrO	TiO ₂	LOI	Total
HTSI-9		15.38	0.03	3.02	0.02	10.25	2.97	5.15	0.10	2.27	0.19	56.53	0.01	0.60	3.09	99.60
HTSI-11		16.67	0.02	8.65	0.02	8.75	0.34	5.00	0.13	3.54	0.10	55.40	0.01	0.52	0.72	99.87
HTSM-1		16.34	0.03	7.07	0.01	9.92	0.99	3.90	0.14	3.71	0.23	54.75	0.02	0.85	1.84	99.80
HTSM-4		15.99	0.02	7.82	<0.01	12.56	0.64	3.17	0.19	3.46	0.18	53.10	0.02	1.21	1.54	99.90
HTSM-8		14.25	0.04	8.34	0.02	13.21	0.93	5.26	0.20	3.76	0.34	47.85	0.04	2.44	3.19	99.86
HTSM-9		14.81	0.03	11.57	0.06	12.58	0.94	7.42	0.22	2.49	0.05	47.63	0.03	0.68	1.37	99.88
No.	La	Ce	Pr	Nd	Sm	Eu	Gd	Tb	Dy	Ho	Er	Tm	Yb	Lu	Co	
HTSI-9	11.20	22.50	2.62	10.40	2.30	0.58	2.14	0.35	2.06	0.41	1.15	0.18	1.06	0.16	30.60	
HTSI-11	6.80	14.50	1.89	8.00	1.94	0.68	1.99	0.36	2.07	0.45	1.31	0.20	1.39	0.20	27.80	
HTSM-1	12.10	30.80	4.41	19.70	4.52	1.07	4.23	0.67	3.96	0.81	2.31	0.35	2.35	0.36	30.90	
HTSM-4	6.50	18.30	2.69	12.60	3.60	1.23	4.48	0.76	4.70	1.03	3.11	0.46	2.91	0.45	34.50	
HTSM-8	28.30	65.80	9.22	39.40	8.81	2.66	8.65	1.28	7.06	1.45	3.69	0.50	3.21	0.46	35.00	
HTSM-9	7.50	20.80	3.12	13.90	4.03	0.79	3.65	0.63	4.00	0.85	2.35	0.34	2.36	0.37	47.70	
No.	Ni	Cu	Zr	Sr	Y	Zn	Cs	Ba	Pb	U	V	Cr	Rb	Ga	Hf	
HTSI-9	50.30	55.00	39.80	118.50	9.70	366.00	4.93	216.00	35.90	0.28	103.00	122.00	105.25	16.30	1.05	
HTSI-11	77.80	10.90	48.10	154.00	12.60	77.00	0.20	59.30	2.50	0.22	165.00	75.00	3.55	16.20	1.40	
HTSM-1	45.40	33.00	69.80	233.00	21.60	78.00	0.37	198.00	3.60	0.13	178.00	61.00	42.70	19.85	2.00	
HTSM-4	34.10	26.80	109.00	178.00	26.00	155.00	0.32	80.00	1.70	0.20	229.00	20.00	13.10	19.40	3.00	
HTSM-8	57.30	33.10	267.00	374.00	36.40	131.00	0.48	277.00	3.00	0.40	245.00	180.00	34.60	25.30	6.50	
HTSM-9	130.00	67.10	29.15	264.50	21.95	222.00	0.35	143.00	6.90	0.22	245.00	203.00	12.55	18.95	1.15	
No.	Ta	Th	Nb	P	Ti	K	ΣREE	ΣLREE	ΣHREE	δEu	δCe	(La:Sm) _N	(La:Yb) _N	(Sm:Nd) _N	(Gd:Yb) _N	
HTSI-9	0.30	2.12	6.30	860.00	3597.00	24,654.86	57.11	49.60	7.51	0.79	0.97	3.06	7.12	0.68	1.63	
HTSI-11	0.22	0.74	3.35	450.00	3117.40	2822.44	41.78	33.81	7.97	1.05	0.96	2.20	3.30	0.75	1.16	
HTSM-1	0.26	0.66	4.95	990.00	5095.75	8218.29	87.64	72.60	15.04	0.74	1.01	1.68	3.47	0.71	1.45	
HTSM-4	0.31	0.50	4.80	790.00	7253.95	5312.83	62.82	44.92	17.90	0.94	1.05	1.14	1.51	0.88	1.24	
HTSM-8	1.30	3.76	21.20	1490.00	14,627.80	7720.21	180.49	154.19	26.30	0.92	0.98	2.02	5.94	0.69	2.17	
HTSM-9	0.33	0.48	5.00	220.00	4076.60	7803.22	64.69	50.14	14.55	0.62	1.03	1.17	2.14	0.89	1.25	
Rock Type		Biotite-Rich Gneiss														
No.	Al ₂ O ₃	BaO	CaO	Cr ₂ O ₃	Fe ₂ O ₃ T	K ₂ O	MgO	MnO	Na ₂ O	P ₂ O ₅	SiO ₂	SrO	TiO ₂	LOI	Total	
HTSF-1	6.94	0.05	1.03	0.01	2.42	1.44	0.33	0.02	1.93	0.05	84.42	<0.01	0.16	0.93	99.73	
HTSF-2	9.53	0.01	2.08	<0.01	2.27	1.02	0.54	0.02	3.33	0.03	78.92	<0.01	0.10	2.06	99.93	
HTSF-4	11.63	0.01	0.77	<0.01	2.14	0.74	1.34	0.02	5.19	0.09	77.36	0.01	0.12	0.63	100.05	
HTSF-5	12.75	0.06	1.45	<0.01	1.64	2.29	0.40	0.02	4.46	0.02	75.21	0.01	0.12	1.67	100.10	
HTSF-10	14.00	0.02	3.14	<0.01	2.80	0.90	1.06	0.02	3.94	0.05	72.28	0.01	0.27	1.24	99.73	
HTSF-11	13.33	0.28	1.71	<0.01	2.48	2.91	0.45	0.02	4.16	0.25	72.19	0.01	0.21	1.03	99.03	
HTSF-14	14.30	0.08	2.34	0.02	4.09	2.43	0.66	0.06	4.14	0.10	68.55	0.04	0.28	1.40	100.00	
HTSF-15	15.92	0.03	3.04	0.01	2.82	1.32	1.05	0.02	5.12	0.16	68.53	0.05	0.28	1.44	99.79	
HTSF-16	14.86	0.03	3.53	<0.01	5.51	1.02	1.53	0.08	4.54	0.07	66.80	0.04	0.40	1.40	99.83	
HTSF-17	15.74	0.08	2.98	0.01	4.59	1.86	1.75	0.07	4.66	0.18	66.01	0.08	0.41	1.68	100.10	
HTSF-18	16.46	0.05	2.70	0.01	3.32	1.21	1.82	0.04	5.85	0.19	65.82	0.08	0.55	1.74	99.84	
HTSF-19	14.33	0.09	2.28	0.01	4.13	3.59	1.61	0.05	3.77	0.15	65.56	0.04	0.34	3.90	99.85	
HTSI-1	13.58	0.04	2.22	0.01	6.76	2.54	3.66	0.11	3.12	0.04	64.64	0.01	0.47	1.90	99.09	
HTSI-2	14.91	0.11	4.84	0.04	5.22	2.62	4.79	0.07	4.17	0.20	59.84	0.07	0.61	2.36	99.85	
No.	La	Ce	Pr	Nd	Sm	Eu	Gd	Tb	Dy	Ho	Er	Tm	Yb	Lu	Co	
HTSF-1	5.20	10.90	1.35	4.90	1.13	0.30	1.12	0.17	0.76	0.11	0.28	0.03	0.18	0.04	3.00	
HTSF-2	29.10	52.40	5.98	20.40	3.45	0.55	2.82	0.49	2.90	0.60	1.66	0.27	1.65	0.27	2.80	
HTSF-4	28.20	60.60	6.78	28.20	6.00	1.45	6.69	1.19	6.74	1.49	4.15	0.67	4.05	0.70	3.90	
HTSF-5	19.60	32.40	3.09	9.70	1.60	0.49	1.33	0.16	0.85	0.15	0.37	0.07	0.36	0.05	2.60	
HTSF-10	3.60	6.80	0.75	2.80	0.72	0.58	0.66	0.11	0.61	0.13	0.39	0.05	0.43	0.08	6.80	
HTSF-11	15.20	31.90	3.98	15.70	3.71	0.89	3.61	0.58	2.67	0.41	0.84	0.11	0.51	0.08	3.00	
HTSF-14	25.60	43.60	4.54	14.80	2.05	0.60	1.41	0.18	1.07	0.22	0.56	0.09	0.67	0.10	11.80	
HTSF-15	17.10	32.60	3.41	11.70	1.52	0.50	0.76	0.09	0.35	0.06	0.15	0.03	0.19	0.02	7.40	
HTSF-16	12.40	25.30	3.08	11.70	2.61	0.61	2.62	0.48	2.97	0.65	2.05	0.35	2.57	0.46	10.90	
HTSF-17	26.00	56.20	6.34	23.60	4.33	1.06	2.96	0.40	1.95	0.40	0.97	0.14	0.84	0.13	11.20	
HTSF-18	7.40	13.70	1.56	5.50	0.82	0.55	0.50	0.06	0.26	0.05	0.13	0.02	0.16	0.02	11.90	
HTSF-19	37.90	73.00	7.56	26.20	4.01	0.83	2.62	0.35	1.90	0.38	1.08	0.15	0.96	0.16	9.50	
HTSI-1	34.50	78.70	9.82	38.80	9.02	1.22	9.85	1.75	10.55	2.36	6.85	0.99	6.58	0.96	14.20	
HTSI-2	22.70	41.90	4.49	17.10	3.42	0.92	2.50	0.36	1.94	0.40	1.08	0.15	0.88	0.15	19.90	
No.	Ni	Cu	Zr	Sr	Y	Zn	Cs	Ba	Pb	U	V	Cr	Rb	Ga	Hf	
HTSF-1	4.00	27.50	88.00	47.30	3.20	65.00	0.80	358.00	4.20	0.30	13.00	70.00	23.70	8.56	2.40	
HTSF-2	2.90	35.50	144.55	64.70	14.40	44.00	0.48	78.70	4.70	0.16	9.00	49.00	25.00	9.84	3.60	
HTSF-4	2.10	24.50	225.00	62.00	8.20	94.00	0.57	110.00	34.30	0.50	24.00	20.00	14.10	13.25	7.00	
HTSF-5	2.40	8.70	104.00	110.50	3.50	22.00	0.91	520.00	3.80	0.30	13.00	20.00	54.10	12.45	3.50	
HTSF-10	7.20	28.70	243.00	132.50	3.60	123.00	2.17	124.00	4.40	0.30	45.00	50.00	38.10	14.35	6.50	
HTSF-11	3.90	4.50	144.00	135.00	11.30	66.00	0.61	2810.00	10.10	0.70	16.00	50.00	40.60	13.25	3.60	
HTSF-14	39.90	9.00	80.15	357.00	5.90	57.00	3.04	652.50	13.20	2.08	51.00	151.00	85.70	19.15	2.20	
HTSF-15	10.80	14.90	89.75	485.00	1.55	38.00	2.07	168.75	8.50	0.31	31.00	46.00	65.25	18.70	2.30	
HTSF-16	12.50	2														

References

- Zhai, M.; Yang, R.; Lu, W.; Zhou, J. Geochemistry and evolution of the Qingyuan Archaean granite—Greenstone terrain, NE China. *Precambrian Res.* **1985**, *27*, 37–62. [[CrossRef](#)]
- Gu, L.; Zheng, Y.; Tang, X.; Zaw, K.; Della-Pasque, F.; Wu, C.; Tian, Z.; Lu, J.; Ni, P.; Li, X. Copper, gold and silver enrichment in ore mylonites within massive sulphide orebodies at Hongtoushan VHMS deposit, N.E. China. *Ore Geol. Rev.* **2007**, *30*, 1–29. [[CrossRef](#)]
- Pei, R.; Wu, L.; Zhao, Y.; Rui, Z.; Zhang, H.; Ye, Q.; Dong, J. *Mineral Deposit Models of China*; Geological Publishing House: Beijing, China, 1995; pp. 331–336.
- Zhang, Q.; Li, S.; Liu, L. *Geology and Metallogeny of the Early Precambrian in China*; Jilin People's Publishing House: Changchun, China, 1984; pp. 295–297.
- Zhang, Y. Study on the Geological Features and Metallogenetic Model of Hongtoushan Copper-Zinc Deposit, Liaoning Province. Master's Thesis, Jilin University, Changchun, China, 2010. (In Chinese with English abstract)
- Franklin, J.M.; Gibson, H.L.; Jonasson, I.R.; Galley, A.G. *Volcanogenic Massive Sulfide Deposits*; Society of Economic Geologists: Littleton, CO, USA, 2005; Volume 98, pp. 523–560. [[CrossRef](#)]
- Wu, K.K.; Zhao, G.; Sun, M.; Yin, C.; He, Y.; Tam, P.Y. Metamorphism of the northern Liaoning Complex: Implications for the tectonic evolution of Neoarchean basement of the Eastern Block, North China Craton. *Geosci. Front.* **2013**, *4*, 305–320. [[CrossRef](#)]
- Li, J.; Shen, B. Geochronology of Precambrian continental crust in Liaoning Province and Jilin Province. *Prog. Precambrian Res.* **2000**, *23*, 242–249.
- Wan, Y.; Liu, D.; Song, B.; Wu, J.; Yang, C.; Zhang, Z.; Geng, Y. Geochemical and Nd isotopic compositions of 3.8 Ga meta-quartz dioritic and trondhjemite rocks from the Anshan area and their geological significance. *J. Asian Earth Sci.* **2005**, *24*, 563–575. [[CrossRef](#)]
- Zhao, G.; Wilde, S.A.; Cawood, P.A.; Lu, L. Thermal Evolution of Archean Basement Rocks from the Eastern Part of the North China Craton and Its Bearing on Tectonic Setting. *Int. Geol. Rev.* **1998**, *40*, 706–721. [[CrossRef](#)]
- Li, Z.; Shan, X.; Liu, J.; Zhang, J.; Liu, Z.; Cheng, C.; Wang, Z.; Zhao, C.; Yu, H. Late Neoarchean TTG and monzogranite in the northeastern North China Craton: Implications for partial melting of a thickened lower crust. *Gondwana Res.* **2023**, *115*, 201–223. [[CrossRef](#)]
- Liu, D.; Nutman, A.; Compston, W.; Wu, J.; Shen, Q.H. Remnants of ≥ 3800 Ma crust in the Chinese part of the Sino-Korean craton. *Geology* **1992**, *20*, 339–342. [[CrossRef](#)]
- Song, B.; Nutman, A.P.; Liu, D.; Wu, J. 3800 to 2500 Ma crustal evolution in the Anshan area of Liaoning Province, northeastern China. *Precambrian Res.* **1996**, *78*, 79–94. [[CrossRef](#)]
- Grant, M.L.; Wilde, S.A.; Wu, F.; Yang, J. The application of zircon cathodoluminescence imaging, Th–U–Pb chemistry and U–Pb ages in interpreting discrete magmatic and high-grade metamorphic events in the North China Craton at the Archean/Proterozoic boundary. *Chem. Geol.* **2009**, *261*, 155–171. [[CrossRef](#)]
- Jahn, B.M.; Zhang, Z.Q. Archean granulite gneisses from eastern Hebei Province, China: Rare earth geochemistry and tectonic implications. *Contrib. Mineral. Petrol.* **1984**, *85*, 224–243. [[CrossRef](#)]
- Wan, Y.; Liu, D.; Wang, W.; Song, T.; Kröner, A.; Dong, C.; Zhou, H.; Yin, X. Provenance of Meso- to Neoproterozoic cover sediments at the Ming Tombs, Beijing, North China Craton: An integrated study of U–Pb dating and Hf isotopic measurement of detrital zircons and whole-rock geochemistry. *Gondwana Res.* **2011**, *20*, 219–242. [[CrossRef](#)]
- Zhao, G.; Wilde, S.A.; Cawood, P.A.; Sun, M. Archean blocks and their boundaries in the North China Craton: Lithological, geochemical, structural and P–T path constraints and tectonic evolution. *Precambrian Res.* **2001**, *107*, 45–73. [[CrossRef](#)]
- Shen, Q. *Early Precambrian Granulites of China*; Geological Publishing House: Beijing, China, 1994.
- Wang, F.P.; Pelletier, S.W. Diterpenoid Alkaloids from Aconitum crassicaule. *J. Nat. Prod.* **1987**, *50*, 55–62. [[CrossRef](#)]
- Zhai, M. Cratonicization and the Ancient North China Continent: A summary and review. *Sci. China Earth Sci.* **2011**, *54*, 1110–1120. [[CrossRef](#)]
- Zhai, M. Major and trace element geochemistry of the Archean Qingyuan granite-greenstone terrane. *Geol. Rev.* **1984**, *30*, 523–535. [[CrossRef](#)]
- Yu, F.; Wang, E.; Yan, P.; Yang, T.; Zhang, R. Geochemical characteristics and prospecting significance of Hongtoushan massive sulfide copper-zinc deposit. *Miner. Resour. Geol.* **2005**, *19*, 117–121. [[CrossRef](#)]
- Yang, Z.S. Poly-deformation of the Archean greenstone belt in the Hongtoushan area, Northern Liaoning province. *Bull. Changchun Coll. Geol.* **1984**, *1*, 20–35.
- Zhao, Y.X. Mineralogy and P–T conditions of crystallization of Archean metamorphic complex from Qingyuan district, Liaoning Province. *J. Changchun Univ. Earth Sci.* **1987**, *1*, 191–204.
- Zhu, M.T.; Zhang, L.C.; Dai, Y.P.; Wang, C.L. In situ zircon U–Pb dating and O isotopes of the Neoarchean Hongtoushan VMS Cu–Zn deposit in the North China Craton: Implication for the ore genesis. *Ore Geol. Rev.* **2015**, *67*, 354–367. [[CrossRef](#)]
- GB/T 14506.28-2010; Methods for Chemical Analysis of Silicate Rocks. Part 28: Determination of 16 Major and Minor Elements Content. National Standardization Technical Committee of Land and Resources: Beijing, China, 2010.
- DZ/T0223-2001; General Principles of Inductively Coupled Plasma Mass Spectrometry (ICP-MS) Analysis. National Standardization Technical Committee of Land and Resources: Beijing, China, 2001.

28. Jackson, S.E.; Pearson, N.J.; Griffin, W.L.; Belousova, E.A. The application of laser ablation-inductively coupled plasma-mass spectrometry to in situ U-Pb zircon geochronology. *Chem. Geol.* **2004**, *211*, 47–69. [[CrossRef](#)]
29. Wiedenbeck, M.A.P.C.; Alle, P.; Corfu, F.Y.; Griffin, W.L.; Meier, M.; Oberli, F.V.; Quadt, A.V.; Roddick, J.C.; Spiegel, W. Three Natural Zircon Standards For U-Th-Pb, Lu-Hf, Trace Element and Ree Analyses. *Geostand. Newsl.* **1995**, *19*, 1–23. [[CrossRef](#)]
30. Paton, C.; Woodhead, J.D.; Hellstrom, J.C.; Hergt, J.M.; Greig, A.; Maas, R. Improved laser ablation U-Pb zircon geochronology through robust downhole fractionation correction. *Geochem. Geophys. Geosyst.* **2010**, *11*, 3. [[CrossRef](#)]
31. Sláma, J.; Košler, J.; Condon, D.J.; Crowley, J.L.; Gerdes, A.; Hanchar, J.M.; Horstwood, M.S.; Morris, G.A.; Nasdala, L.; Norberg, N.; et al. Plešovice zircon—A new natural reference material for U-Pb and Hf isotopic microanalysis. *Chem. Geol.* **2008**, *249*, 1–35. [[CrossRef](#)]
32. Liu, Y.; Gao, S.; Hu, Z.; Gao, C.; Zong, K.; Wang, D. Continental and Oceanic Crust Recycling-induced Melt–Peridotite Interactions in the Trans-North China Orogen: U-Pb Dating, Hf Isotopes and Trace Elements in Zircons from Mantle Xenoliths. *J. Petrol.* **2009**, *51*, 537–571. [[CrossRef](#)]
33. Vermeesch, P. IsoplotR: A free and open toolbox for geochronology. *Geosci. Front.* **2018**, *9*, 1479–1493. [[CrossRef](#)]
34. Hou, K.; Li, Y.; Tian, Y. In situ U-Pb zircon dating using laser ablation-multi ion counting-ICP-MS. *Miner. Depos.* **2009**, *28*, 481–492. [[CrossRef](#)]
35. Gerdes, A.; Zeh, A. Combined U-Pb and Hf isotope LA-(MC-) ICP-MS analyses of detrital zircons: Comparison with SHRIMP and new constraints for the provenance and age of an Armorican metasediment in Central Germany. *Earth Planet. Sci. Lett.* **2006**, *249*, 47–61. [[CrossRef](#)]
36. Koglin, N.; Kostopoulos, D.; Reischmann, T. The Lesvos mafic-ultramafic complex, Greece: Ophiolite or incipient rift? *Lithos* **2009**, *108*, 243–261. [[CrossRef](#)]
37. Mojzsis, S.J.; Harrison, T.M.; Pidgeon, R.T. Oxygen-isotope evidence from ancient zircons for liquid water at the Earth's surface 4,300 Myr ago. *Nature* **2001**, *409*, 178–181. [[CrossRef](#)]
38. Polat, A.; Hofmann, A. Alteration and geochemical patterns in the 3.7–3.8 Ga Isua greenstone belt, West Greenland. *Precambrian Res.* **2003**, *126*, 197–218. [[CrossRef](#)]
39. Large, R.R.; Gemmell, J.B.; Paulick, H.; Huston, D.L. The alteration box plot: A simple approach to understanding the relationship between alteration mineralogy and lithogeochemistry associated with volcanic-hosted massive sulfide deposits. *Econ. Geol.* **2001**, *96*, 957–971. [[CrossRef](#)]
40. Pearce, J.A.; van der Laan, S.R.; Arculus, R.J.; Murton, B.J.; Ishii, T.; Peate, D.W.; Parkinson, I.J. Boninite and harzburgite from Leg 125 (Bonin-Mariana forearc): A case study of magma genesis during the initial stages of subduction. In *Proceedings of the Ocean Drilling Program, Scientific Results*; Citeseer: Forest Grove, OR, USA, 1992; Volume 125, pp. 623–659. [[CrossRef](#)]
41. Sun, S.S.; McDonough, W.F. Chemical and isotopic systematics of oceanic basalts: Implications for mantle composition and processes. *Geol. Soc. Lond. Spec. Publ.* **1989**, *42*, 313–345. [[CrossRef](#)]
42. Winchester, J.; Floyd, P. Geochemical discrimination of different magma series and their differentiation products using immobile elements. *Chem. Geol.* **1977**, *20*, 325–343. [[CrossRef](#)]
43. Hawkesworth, C.; Rogers, N.; Van Calsteren, P.; Menzies, M. Mantle enrichment processes. *Nature* **1984**, *311*, 331–335. [[CrossRef](#)]
44. Mahoney, J.J. *Continental Flood Basalts*; Springer Science & Business Media: Berlin, Germany, 1988; pp. 151–194. [[CrossRef](#)]
45. Carlson, R. Physical and chemical evidence on the cause and source characteristics of flood basalt volcanism. *Aust. J. Earth Sci.* **1991**, *38*, 525–544. [[CrossRef](#)]
46. Hergt, J.; Peate, D.; Hawkesworth, C. The petrogenesis of Mesozoic Gondwana low-Ti flood basalts. *Earth Planet. Sci. Lett.* **1991**, *105*, 134–148. [[CrossRef](#)]
47. Arndt, N.T.; Christensen, U. The role of lithospheric mantle in continental flood volcanism: thermal and geochemical constraints. *J. Geophys. Res. Solid Earth* **1992**, *97*, 10967–10981. [[CrossRef](#)]
48. Gallagher, K.; Hawkesworth, C. Dehydration melting and the generation of continental flood basalts. *Nature* **1992**, *358*, 57–59. [[CrossRef](#)]
49. Saunders, A.; Storey, M.; Kent, R.; Norry, M. Consequences of plume-lithosphere interactions. *Geol. Soc. Lond. Spec. Publ.* **1992**, *68*, 41–60. [[CrossRef](#)]
50. Arndt, N.T.; Czamanske, G.K.; Wooden, J.L.; Fedorenko, V.A. Mantle and crustal contributions to continental flood volcanism. *Tectonophysics* **1993**, *223*, 39–52. [[CrossRef](#)]
51. Puchtel, I.; Arndt, N.; Hofmann, A.; Haase, K.; Kröner, A.; Kulikov, V.; Kulikova, V.; Garbe-Schönberg, C.D.; Nemchin, A. Petrology of mafic lavas within the Onega plateau, central Karelia: evidence for 2.0 Ga plume-related continental crustal growth in the Baltic Shield. *Contrib. Mineral. Petrol.* **1998**, *130*, 134–153. [[CrossRef](#)]
52. Ernst, R.E.; Buchan, K.L.; Campbell, I.H. Frontiers in large igneous province research. *Lithos* **2005**, *79*, 271–297. [[CrossRef](#)]
53. Hari, K.R.; Swarnkar, V.; Prasanth, M.P.M. Significance of assimilation and fractional crystallization (AFC) process in the generation of basaltic lava flows from Chhotaudepur area, Deccan Large Igneous Province, NW India. *J. Earth Syst. Sci.* **2018**, *127*, 85. [[CrossRef](#)]
54. McDonough, W. Constraints on the composition of the continental lithospheric mantle. *Earth Planet. Sci. Lett.* **1990**, *101*, 1–18. [[CrossRef](#)]
55. Pearce, J.A. Geochemical fingerprinting of oceanic basalts with applications to ophiolite classification and the search for Archean oceanic crust. *Lithos* **2008**, *100*, 14–48. [[CrossRef](#)]

56. Piercy, S.J.; Mortensen, J.K.; Murphy, D.C.; Paradis, S.; Creaser, R.A. Geochemistry and tectonic significance of alkalic mafic magmatism in the yukon-tanana terrane, finlayson lake region, yukon. *Can. J. Earth Sci.* **2002**, *39*, 1729–1744. [[CrossRef](#)]
57. Condie, K.C. High field strength element ratios in Archean basalts: A window to evolving sources of mantle plumes? *Lithos* **2005**, *79*, 491–504. [[CrossRef](#)]
58. Cook, Y.; Sanislav, I.; Hammerli, J.; Blenkinsop, T.; Dirks, P. A primitive mantle source for the Neoarchean mafic rocks from the Tanzania Craton. *Geosci. Front.* **2016**, *7*, 911–926. [[CrossRef](#)]
59. Hart, T.; Gibson, H.; Lesher, C. Trace element geochemistry and petrogenesis of felsic volcanic rocks associated with volcanogenic massive Cu-Zn-Pb sulfide deposits. *Econ. Geol.* **2004**, *99*, 1003–1013. [[CrossRef](#)]
60. Lesher, C.M.; Goodwin, A.M.; Campbell, I.H.; Gorton, M.P. Trace-element geochemistry of ore-associated and barren, felsic metavolcanic rocks in the Superior Province, Canada. *Can. J. Earth Sci.* **1986**, *23*, 222–237. [[CrossRef](#)]
61. Piercy, S. An overview of petrochemistry in the regional exploration for volcanogenic massive sulphide (VMS) deposits. *Geochem. Explor. Environ. Anal.* **2010**, *10*, 119–136. [[CrossRef](#)]
62. Cathles, L.M.; Erindi, A.; Barrie, T. How long can a hydrothermal system be sustained by a single intrusive event? *Econ. Geol.* **1997**, *92*, 766–771. [[CrossRef](#)]
63. Barrie, C.; Hannington, M. Classification of volcanic-associated massive sulfide deposits based on host-rock composition. *Rev. Econ. Geol.* **1999**, *8*, 1–11. [[CrossRef](#)]
64. Liu, Z. A comment on “In situ zircon U-Pb dating and O isotopes of the Neoarchean Hongtoushan VMS Cu-Zn deposit in the North China Craton: Implication for the ore genesis” by Ming-Tian Zhu et al. [Ore Geol. Rev. 67 (2015) 354–367]. *Ore Geol. Rev.* **2018**, *95*, 1179–1180. [[CrossRef](#)]
65. Rollinson, H. *Using Geochemical Data: Evaluation, Presentation, Interpretation*; Longman: London, UK, 1993; Volume 1. [[CrossRef](#)]
66. Hawkesworth, C.; Kemp, A. Using hafnium and oxygen isotopes in zircons to unravel the record of crustal evolution. *Chem. Geol.* **2006**, *226*, 144–162. [[CrossRef](#)]
67. Zhu, M.; Zhang, L.; Dai, Y.; Wang, C.; Peng, Z. Hydrothermal modification of zircon geochemistry and Lu-Hf isotopes from the Hongtoushan Cu-Zn deposit, China. *Ore Geol. Rev.* **2017**, *86*, 707–718. [[CrossRef](#)]
68. Wan, Y.; Liu, D.; Wang, S.; Dong, C.; Yang, E.; Wang, W.; Zhou, H.; Ning, Z.; Du, L.; Yin, X.; et al. Juvenile magmatism and crustal recycling at the end of the Neoarchean in Western Shandong Province, North China Craton: Evidence from SHRIMP zircon dating. *Am. J. Sci.* **2010**, *310*, 1503–1552. [[CrossRef](#)]
69. Zhao, G.; Wilde, S.A.; Cawood, P.A.; Lu, L. Thermal evolution of two textural types of mafic granulites in the North China craton: Evidence for both mantle plume and collisional tectonics. *Geol. Mag.* **1999**, *136*, 223–240. [[CrossRef](#)]
70. Wu, F.; Zhao, G.; Wilde, S.A.; Sun, D. Nd isotopic constraints on crustal formation in the North China Craton. *J. Asian Earth Sci.* **2005**, *24*, 523–545. [[CrossRef](#)]
71. Su, B.X.; Su, B.X. Permian Mantle Plume and Paleozoic Tectonic Evolution. In *Mafic-Ultramafic Intrusions in Beishan and Eastern Tianshan at Southern CAOB: Petrogenesis, Mineralization and Tectonic Implication*; Springer: Berlin/Heidelberg, Germany, 2014; pp. 183–207.
72. Heaman, L.M. Global mafic magmatism at 2.45 Ga: Remnants of an ancient large igneous province? *Geology* **1997**, *25*, 299–302. [[CrossRef](#)]
73. Isley, A.E.; Abbott, D.H. Plume-related mafic volcanism and the deposition of banded iron formation. *J. Geophys. Res. Solid Earth* **1999**, *104*, 15461–15477. [[CrossRef](#)]
74. Griffin, W.; Pearson, N.; Belousova, E.; Jackson, S.v.; Van Achterbergh, E.; O'Reilly, S.Y.; Shee, S. The Hf isotope composition of cratonic mantle: LAM-MC-ICPMS analysis of zircon megacrysts in kimberlites. *Geochim. Cosmochim. Acta* **2000**, *64*, 133–147. [[CrossRef](#)]
75. Wan, Y.; Xie, H.; Yang, H.; Wang, Z.; Liu, D.; Kroner, A.; Wilde, S.A.; Geng, Y.; Sun, L.; Ma, M. Is the Ordos Block Archean or Paleoproterozoic in age? Implications for the Precambrian evolution of the North China Craton. *Am. J. Sci.* **2013**, *313*, 683–711. [[CrossRef](#)]
76. Blichert-Toft, J.; Albarède, F. The Lu-Hf isotope geochemistry of chondrites and the evolution of the mantle-crust system. *Earth Planet. Sci. Lett.* **1997**, *148*, 243–258. [[CrossRef](#)]
77. Nowell, G.; Kempton, P.; Noble, S.; Fitton, J.; Saunders, A.; Mahoney, J.; Taylor, R. High precision Hf isotope measurements of MORB and OIB by thermal ionisation mass spectrometry: Insights into the depleted mantle. *Chem. Geol.* **1998**, *149*, 211–233. [[CrossRef](#)]

Disclaimer/Publisher’s Note: The statements, opinions and data contained in all publications are solely those of the individual author(s) and contributor(s) and not of MDPI and/or the editor(s). MDPI and/or the editor(s) disclaim responsibility for any injury to people or property resulting from any ideas, methods, instructions or products referred to in the content.